Simulation of Premixed Turbulent Combustion Based on the Eulerian Flame Tracking model

Master Student: **Yanni Wang**

Advisor AVL: **Dipl. -Ing. Dr. Peter Priesching**

Advisor TU Graz: **Prof. Dipl.-Ing. Dr. Andreas Wimmer**

September 8, 2018

Acknowledgment

First and foremost, I would like to express my sincere gratitude to my supervisor Dr. Peter Priesching at AVL for his guidance and support. From his detailed answer to my inquiry about the master thesis at the end of 2016, to his careful suggestions and modifications about the writing, what he did always motivated and inspired me. Because of his help I experienced a very pleasant office atmosphere during this period. I appreciate all his contributions of time, suggestions and ideas regarding all aspects of the combustion theory and the CFD modeling.

I would also like to thank Dr. Jooyoung Hahn for his explanation of the mathematical background of the 3D-CFD modeling and programming techniques. He always came to me whenever I had a question about my simulations.

My sincere thanks to my supervisor Prof. Andreas Wimmer at TU Graz. I am gratefully indebted to his very valuable comments on this thesis.

I would also like to acknowledge Prof. Liguang Li at Tongji University for his careful guidance. The enthusiasm he has for his research in the combustion area motivated me. Many thanks to Dr. Haifeng Lu for providing the experimental data of the combustion vessel case.

I would like to express my deepest appreciation towards AVL, TU Graz and Tongji University for this double-master program. Otherwise I could not get this chance to study and write my master thesis in Graz.

Finally, and most importantly, I would like to thank my family. Without their support I could not focus on my study and research. Thanks a lot for their unconditional love and accompany.

Abstract

The goal of this thesis is to evaluate the new combustion model, Eulerian Flame Tracking Model (a kind of level-set based flamelet model) by calculating different academic and engine examples. Special emphasis was put on the mathematical description of the premixed turbulent combustion based on the G-equation (level-set methods). After the successful implementation of the Eulerian Flame Tracking Model to AVL FIRE™, different modeling aspects have been evaluated, e.g. sensitivity to the mesh element size, meshing topology strategies and time step size.

After that, the ability of the model for the prediction of laminar combustion phenomena was evaluated using a cylindrical combustion vessel. The Schlieren images recorded by the high-speed camera were used to assess the prediction ability of the laminar flame front propagation.

The pancake engine with relatively simple geometrical structures was used to evaluate the model. The in-cylinder pressure trace by the pressure transducer and the heat release rate were used to compare with the simulation results.

Finally, the model was validated by reference to the experimental data for an AVL prototype direct injection, spark ignition engine. Various engine operating points were investigated in order to evaluate the effects of engine speed, equivalence ratio, spark timing variations. In-cylinder pressure histories were in good agreement to the measured data. The turbulent flame front propagated reasonably. The reason for the deviation of the simulated heat release rate was given and strategies for improving the accuracy of the Eulerian Flame Tracking Model have been proposed.

Contents

List of figures

List of tables

Nomenclature

ABBREVIATIONS

Symbol	*Meaning*
ATDC	after top dead center
BTDC	before top dead center
BDC	bottom dead center
BMEP	break mean effective pressure
BML	Bray-Moss-Libby
CAD	crankshaft angle degree
CD	combustion duration
CFD	computational fluid dynamics
CFL	Courant-Friedrichs-Lewy condition
CFM	Coherent Flame Model
CMC	conditional moment closure
CVM	constant volume method
DI	direct injection
DISI	direct injection spark ignition
EFTM	Eulerian flame tracking model
EIA	environmental information administration
EGR	exhaust gas recirculation
EOI	end of injection
EV	exhaust valve angle
EVC	exhaust valve closing
EVO	exhaust valve opening
GFWI	G-equation based Flame-Wall Interaction
HCCI	homogenous charge compression ignition
ICE	internal combustion engine
IMEP	indicated mean effective pressure
IPCC	intergovernmental panel on climate change
IV	intake valve angle
IVC	intake valve closing
LEM	linear eddy model
IVO	intake valve opening
LTC	low temperature combustion
MFB50	crank angle of the 50% mass fraction burnt point
ODE	ordinary differential equation
PCCI	premixed charge compression ignition
PDF	probability density function
PFI	port fuel injection
RANS	Reynolds-averaged Navier-Stokes
RCCI	reactivity-controlled compression ignition
RDE	real driving emission

RIF	representative interactive flamelet
SI	spark ignition
SOI	start of injection
SOC	start of combustion
TDC	top dead center

LATIN SYMBOLS

Symbol	*Meaning*	*Unit*
s_T	turbulent burning velocity	m/s
s_P	piston speed	m/s
ℓ	integral turbulent length scale	m
k	turbulence kinetic energy	m^2/s^2
ε	turbulence dissipation rate	m^2/s^3
ρ	unburnt gas mixture density	kg/m^3
λ	thermal conductivity	$W/m/K$
ν	kinematic viscosity of fluid	m^2/s
η	Kolmogorov length scale	m
c_p	specific heat capacity at constant pressure	J/kg/K
D	thermal diffusion coefficient	kg/m/s
γ	gas expansion parameter	-
ℓ_F	flame thickness	m
Da	Damköhler number	-
Ka	Karlovitz number	-
Re	Reynolds number	-
t_F	flame time	s
t_η	Kolmogorov time scale	s
ϕ	equivalence ratio	-
s_L	laminar burning velocity	m/s
ν'	turbulence intensity	m/s
ℓ_δ	thickness of the inner layer	m
τ	integral time scale	s
T	temperature	K
T_w	wall temperature	K
c	progress variable used in BML model	-
Pr	Prandtl number	-
y	distance to the wall	m
y^+	dimensionless distance	-
u^*	friction velocity	m/s
Q_c	volumetric heat release	J/m^3
m_{cyl}	mixture mass in cylinder	kg
m_{in}	mass from the intake port	kg

m_{exh}	mass from the exhaust port	kg
m_f	injected fuel mass	kg
m_b	blowby mass	kg
$\dot{m}_K$	mass stream of the mixture	kg/s
n	engine speed	r/min
α_{SOC}	start of combustion	CAD
$\mathcal{L}$	Markstein length	m
S	strain rate	-
Le	Lewis number	-
ℓ_δ	thickness of the inner layer of the flame structure	m
c	normalized temperature in BML	-
$\dot{\omega}_c$	chemical source term	kg/m^3/s
u_i	velocity term of species i	m/s
ψ	set of stochastic variables	-
Γ	interface defined in the level set approach	-
$\mathbb{R}$	the dimension of the space defined	-
$\phi(x,y,z)$	level set function	-
G	the non-reactive scalar	m
G_0	zero level set of the G-scalar	m
$\boldsymbol{v}_f$	velocity of the flow field	m/s
σ	gradient of G	m
$\tilde{\chi}$	scalar dissipation	1/s
$\widetilde{\omega}$	kinematic restoration	1/s
c_s	modeling constant of equation 4.17	-
Sc_t	turbulent Schmidt number	-
A_T	the instantaneous flame surface area	m^2
A	the cross-sectional area	m^2
D_f	the fractal dimension in equation 4.26	-
r_0	initial radius of the flame kernel	m
CFL	Courant number	-
ΔL	cell length of the mesh	m
Δt	time step used in the simulation	m
T_u	the temperature of the unburnt mixture	K
p_0	initial pressure	Pa
T_0	initial temperature	K
q	heat flux	W/m^2
Q_c	chemical heat release	J
H	enthalpy	J
h	specific enthalpy	J/kg
V	volume	m^3
η_{spk}	efficiency of the heat transferred from the spark	-
$\overline{s_P}$	mean piston speed	m/s
U_w	internal energy	J
LHV	lower heating value	J/kg

$\boldsymbol{x}$	Cartesian coordinate	m,m,m
t	time	s
r_c	the critical radius of the model switch	m

SUBSCRIPTS

Symbol	*Meaning*
b	burnt
b	blow-by
F	mean flame front
f	fuel
th	theoretical
m	measured
cyl	cylinder
w	wall
spk	spark
u	unburnt
p	constant-pressure
l	laminar
t	turbulent
0	initial status

1 Introduction

The ICEs (internal combustion engine) were invented in the 19th century. Through more than one hundred years' development and improvement, they became the most-widely used power machines in industries, transportation and agricultural field etc. In the automotive industry, more than 1.2 billion vehicles are equipped with ICEs currently[1]. The worldwide number of car ownerships is still increasing as shown in Figure 1-1. According to the statistical data from the Annual energy outlook by Energy Information Administration (EIA), the energy consumption in the transportation sector will keep in a relatively high and stable level in next 30 years[2]. Among all kinds of fuels, the consumption rate of the petroleum is and will still be the most dominant one (cf. Figure 1-2). For road traffic usages, gasoline and diesel are two mostly common fuels. The continuously increasing car numbers lead to high energy demands. Although new vehicles driven by clean energy have been developed and series-produced, their market share is still very low (e.g. the share of the clean energy passenger vehicles in China was 1.6% in 2016).

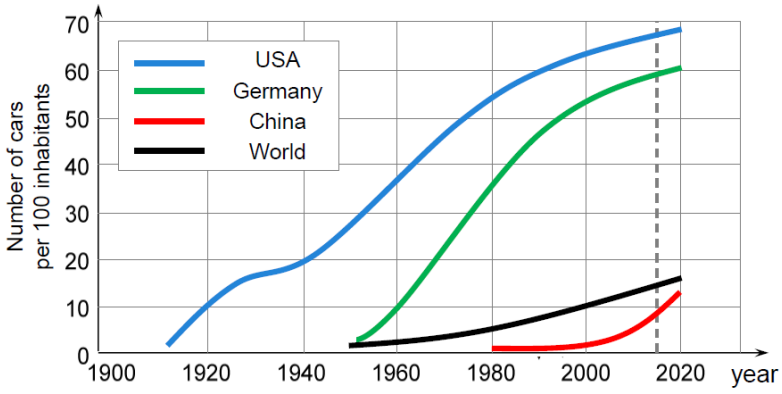

Figure 1-1 Growth of motorization in the whole world[1]

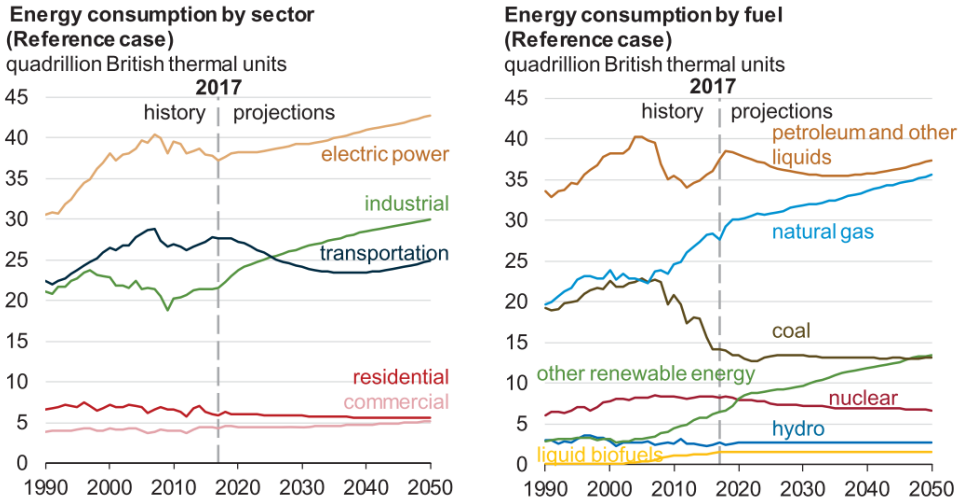

Figure 1-2 Energy consumption changes over the projection period, Annual Energy Outlook 2018[2]

However, the high fossil energy consumption has a large negative influence on the environment, climate, air quality and health. It causes concerns about air pollutions in cities, contributes to the climate change and the global warming. The global CO2 emission has risen from about 22 Gt in 1990 to 36 Gt in 2015, where 94% of the whole CO2 emissions are anthropogenic CO2[3]. In order to reduce the CO2 emission and mitigate the global warming, Intergovernmental Panel on Climate Change (IPCC) recommends that greenhouse gases emitted by human activities should be reduced 40%~70% in 2050 compared to the quantity in 2010. Through this way the global temperature increase can be controlled within 2°C by the end of the 21st century[4]. With the ever-rising need for high fuel consumption, lower CO_2 and other limited emissions, the development of better engine technologies is essential.

Compared to gasoline engines, diesel engines have an obvious lower CO2 emission because of their higher efficiency (see Figure 1-3). The market share of diesel engines is currently more than 50% of new light-duty vehicle registrations in Europe. However, due to the emission scandal, tighter NOx emission standards and the real driving emission (RDE) testing, the diesel market share could decrease in future years[5]. The reducing diesel market share can therefore result in the increase of the market share of cars equipped with gasoline engines.

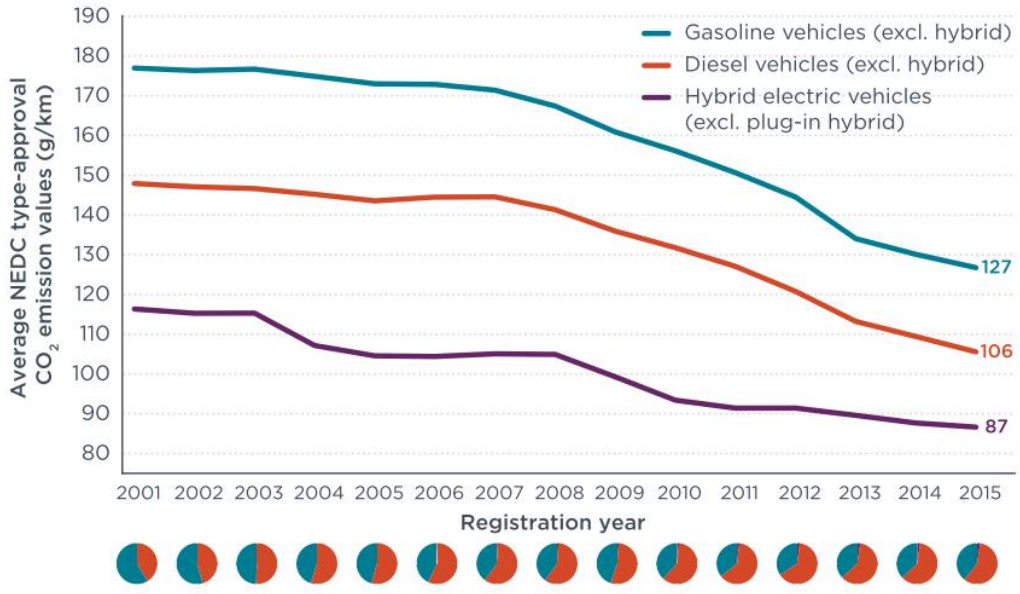

Figure 1-3 Sales-weighted average type-approval CO2 emissions from EU lower medium passenger cars by fueling technology. Pie charts indicate the market share of gasoline, diesel and hybrid vehicles in each year[5]

In China, Japan and US, the light-duty vehicle markets are all dominated by gasoline-fueled cars. As a result, the high-performance gasoline engines are in high-demands. A variety of technologies are being considered to obtain the desired efficiency improvement and the emission reduction. Some examples include using direct fuel injection, downsizing, turbocharging, low temperature combustion[6] (LTC, including e.g. homogeneous charge compression ignition (HCCI), reactivity-controlled

compression ignition (RCCI), premixed charge compression ignition (PCCI) etc.), lean combustion, in-cylinder water-injection etc.
However, within the development process of modern gasoline engines, the number of parameters is increasing continuously. Investigations of all these parameters is challenging using experimental studies alone. Isolating the effect of any design change is difficult without access to temporally and spatially resolved data in the entire engine. Ensuring repeatable initial conditions is also a significant challenge in engine test bench studies. Furthermore, the high costs of physical experiments are unaffordable. Therefore, it is necessary to apply tools like computational fluid dynamics (CFD) since the computational power has been increased dramatically in the last 15 years.
In recent times, CFD has been widely used for the development of ICEs[7][8][9] for the purpose of obtaining higher fuel efficiency and lower emissions. Through CFD tools the derivation of difficultly measurable quantities is possible. Based on the works of other researchers, a good understanding of the in-cylinder turbulent combustion process is one of the key factors for a successful modeling. Therefore, a high-fidelity combustion model is essential for obtaining trustworthy simulation results. The newly developed 'Eulerian Flame Tracking Model' applies a level-set approach to describe the surface of a propagating flame. It's a powerful tool to model both premixed and partially premixed combustion phenomena occurring in SI engines[10].
Based on the Eulerian Flame Tracking Model, the position of the flame surface is known at any time in the cylinder, which makes it possible to calculate the heat release during the whole engine operating cycle, and to investigate the pre- and post-flame effects as well as flame-wall interactions. The engine combustion process becomes trackable. Therefore, the developing costs (e.g. prototype numbers, experiment numbers, etc.) are considerably reduced and the time needed for SoP (Start of Production) is obviously shortened.
During the development of the EFTM model, special cares have been taken of the numerical stability of the method for arbitrary mesh topologies. This fact makes it possible to apply the model to a large number of examples, which are based on different meshing strategies.

The structure and outline of this work is as follows:

1) Chapter 2 introduces the premixed turbulent combustion. The derivation of the typical regime diagram for premixed turbulent combustion is presented.
2) Chapter 3 presents the widely-used turbulent combustion models. Their characteristics are analyzed and the comparison of these models is given.
3) Chapter 4 describes the mathematical background of the G-equation in detail. The level-set approach for determining the flame front location is introduced, followed by the turbulence modeling of the G-equation.
4) A detailed model validation is described in chapter 5. Two academic cases, one combustion vessel case and two SI engine cases are investigated. The simulation results are discussed in detail and are compared to experimental data.
5) In the last chapter, the work of this thesis is summarized and areas for future improvements are highlighted.

2 Premixed Turbulent Combustion

In terms of the state of the flow, combustion processes can be classified in laminar and turbulent. In industrial applications, combustion nearly always takes place within a turbulent rather than a laminar flow field because of two reasons:

1) Turbulence can enhance the mixing processes and therefore enhance the combustion;
2) The releasing heat during combustion processes generates buoyancy or gas expansion which lead to the flow instability. This could enhance the transition of the state of flow fields to turbulence.

According to the combustible mixture formation process, combustion processes can be subdivided in: premixed, non-premixed and partially premixed combustion. In external mixture formation engines and lean-burn gas turbines, the occurring combustion phenomena are classified as premixed. On the contrary, the combustion process in diesel engines produces typical non-premixed flames. Partially premixed combustion phenomena can be observed in the modern stratified charging Direct Injection Spark Ignition (DISI) engine.

Combustion in homogenous charge SI (Spark Ignition) engines or DISI engines with the relatively early fuel injection timing belongs to the premixed turbulent combustion category. Under this condition, fuel and air are mixed by turbulence generated by well-designed intake ports. This mixing process lasts a sufficiently long time before the mixture is ignited by a spark plug. The gaseous combustible mixture in the vicinity of the spark plug is ionized through the deposition of electrical energy from the spark and is heated to thousands of Kelvins. For temperature above 1000K, chemical reactions are initiated, which generate a flame kernel. This flame kernel grows at first laminarly and afterwards turbulently. Therefore, a fundamental review for the laminar and turbulent flame propagation is meaningful for the understanding of the whole combustion process occurring in the combustion chamber. It provides a solid foundation for the numerical implementation of the model and the accurate simulation of the combustion process in SI engines.

2.1 Laminar flame propagation

The understanding of the physics of laminar combustion processes is necessary for investigating the turbulent combustion phenomena based mainly on two reasons.

1) many theories of turbulent combustion models use the assumption that the turbulent flame front consists of an ensemble of laminar flamelets,
2) the flame kernel in the combustion chamber propagates laminarly at the early stage of the whole combustion process.

In laminar combustion processes, transport phenomena are as important as chemistry. Determining the chemical-kinetic parameters is the most challenging part in accurate description of the laminar flames. According to Williams[11], typical uncertainties in estimating the values of kinetic parameters are of the order of 10%. For example, when using Octane as the fuel, the number of reactions is more than 2000. Since at least three parameters in each reaction should be determined, total unknown kinetic

parameters are more than 6000. Therefore, a combustion model embedded with detailed chemical kinetics is still a major difficulty in numerical combustion studies.
The flame structure of the premixed laminar stochiometric CH4-air mixture is shown in Figure 2-1. The flame is divided into three regions:

1) Preheat zone, where the unburnt mixture is preheated. It is assumed to be chemically inert. The thickness of the preheat zone depends only on the molecular transport, since there is no heat release in this layer.
2) Oxidation layer. In this layer, intermediate species produced during the combustion process are oxidized. The thickness of this layer is of order ε (turbulence dissipation). It is not important for the flame characteristics[12].
3) Inner layer. Rate-determining reactions take place in this layer. As a result, this layer is responsible for keeping the reaction process continuously going on so the combustion process. If the turbulence eddies penetrate into this layer, the entire flame structure will be disturbed and the assumption of laminar flamelets is then inappropriate. The thickness of this layer will be discussed more in detail in the section 2.2.1, derivation of the regime diagram for premixed turbulent combustion.

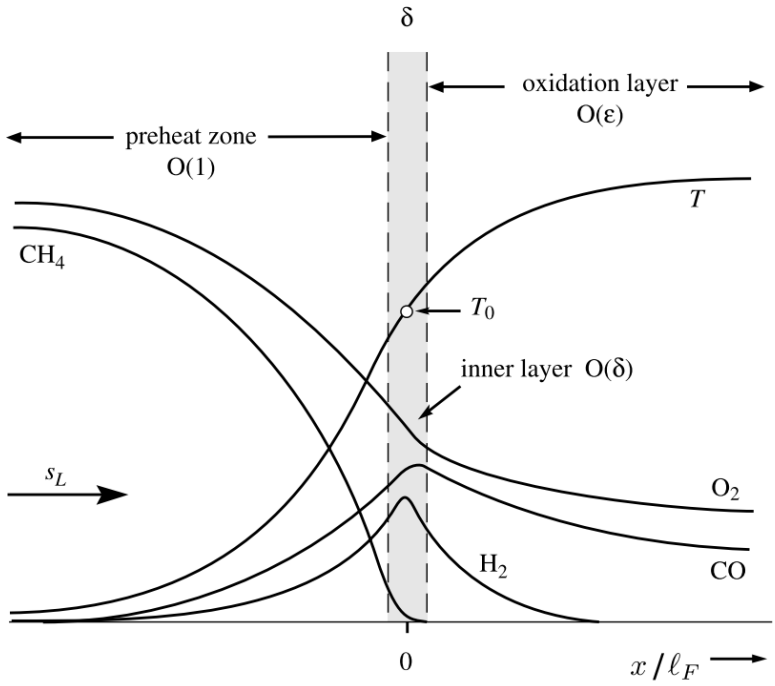

Figure 2-1 Schematic illustration of the structure of a stoichiometric premixed methane-air flamelets[13]

Under the assumption of that the convective transport is equal to the diffusive transport, the flame thickness of premixed flames can be defined as:

$$\ell_F = \frac{D}{s_L^0} = \frac{\lambda / c_p}{(\rho s_L^0)_u} \tag{2.1}$$

where λ is the heat conductivity and c_p the heat capacity evaluated at the inner layer temperature T_0, s_L^0 the unstretched laminar flame burning velocity. It should be noted

that the derivation employed the assumption that heat and species diffused in the same way ($Le = 1$).

Smoke et al.[14] proposed a formula to approximately describe the λ/c_p, which reads as

$$\frac{\lambda}{c_p} = 2.58 \times 10^{-5} \left(\frac{T_0}{298}\right)^{0.7} \tag{2.2}$$

Now the laminar flame thickness can be obtained when the unstretched laminar flame burning velocity s_L^0 is known.

Laminar burning velocity s_L is one of the most important intrinsic properties of a combustible mixture, since it contains the diffusivity, reactivity and other physicochemical information of the mixture. Furthermore, s_L is used as a scaling parameter for the turbulent burning velocity s_T and for the premixed turbulent combustion modeling. The accurate measurement and formulation of s_L play a very important role for the considerable prediction ability of the premixed combustion model. Different methods and approaches have been developed to experimentally measure this quantity.

According to the work of Andrews et al.[15] and Bradley et al.[16], the spherical flames outwardly propagating with the constant peripheral pressure has a clear and well-defined stretch rate that is uniform over the surface, where the burning velocity is defined. Therefore, it is the ideal flame for the investigation of laminar burning velocities. The early stage of the combustion process occurring in a constant volume combustion vessel can also be treated as constant-pressure, since the pressure increasing is still neglectable. Lots of experimental and computational studies of the laminar combustion that based on the constant volume combustion vessel have been carried out by different researchers. The schematic illustration of the common-used combustion vessel is depicted in Figure 2-2.

Metghalchi et al.[17] [18] and coworkers[19] used the cylindrical vessel with the optical access to identify the possible instability and cellular formation appearing in the flame front development. Saeed et al.[20] employed a spherical combustion bomb that both the pressure trace and the flame front history were recorded in experiments. He measured burning rates for methanol (liquidus fuel) at elevated initial temperatures ($T_0 = 425K$) and pressures ($p_0 = 2.0\,\mathrm{bar}, 3.5\,\mathrm{bar}$). Razus et al. [21][22] used a spherical chamber equipped with a pressure sensor to study the characteristics of laminar burning velocities for propane-air mixture. Thereby, only the pressure history was recorded. The spherical combustion vessel with a diameter of 152.9 mm used by Matsugi et al.[23] had both an optical access and one pressure transducer, whereas Xiouris et al. [24]used a bigger one with 203.2 mm diameter to find the laminar burning velocity of methane-air, propane-air and synthesis gas-air mixtures.

Gu et al.[25] employed the combustion vessel to generate spherically expanding flames propagating at the constant pressure, so that the unstretched laminar burning velocity of methane-air mixtures at initial pressures between 0.1 and 1 MPa, and initial temperatures between 300 and 400 K can be derived. Three equivalence ratios, 0.8,

1.0 and 1.2 are studied.

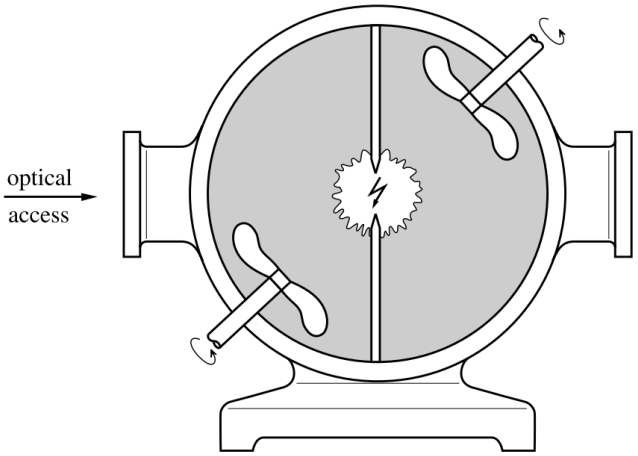

Figure 2-2 Outwardly propagating spherical flame in a combustion vessel[12]

Except for the experimental investigations of the s_L, Bradley et al.[26], Marshall et al.[27] and Saeed et al.[28] also carried out the computational studies. Based on the conclusions gained from previous works of the researchers, the laminar burning velocity s_L is a thermal-chemical transport property that depends mainly on the fuel-air equivalence ratio ϕ, unburnt temperature T_u and pressure p. Figure 2-3 shows the influence of equivalence ration on laminar burning velocity calculated for CH_4-Air by Mauss et. al.[29]. For hydrogen, methanol and other hydrocarbon fuels Peters et. al[30] have given the correlations of the laminar burning velocity.

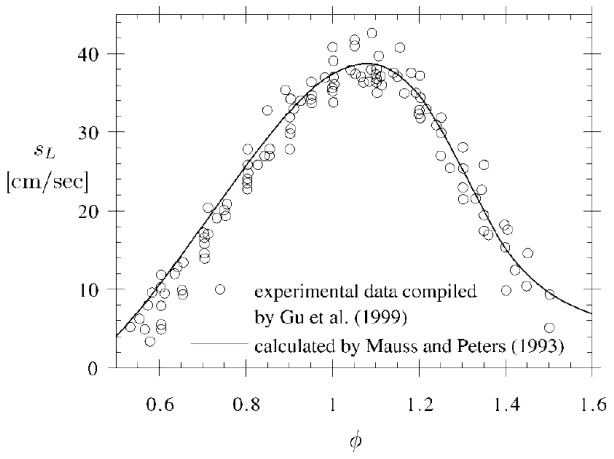

Figure 2-3 Laminar burning velocity of methane air mixture[12]

Corresponding to the definition of the flame thickness (cf. Equation 2.1), the flame time is defined as:

$$t_F = \frac{\ell_F}{s_L} = \frac{D}{s_L^2} \tag{2.3}$$

t_F can be interpreted as the time that the flame needs to propagate over a distance

ℓ_F. In the work of Peters[12], within the region of laminar premixed flames, t_F is equal to the chemical time scale t_c.

When a flame propagates in a three-dimensional space, where the flow field is not uniform, the curvature and strain effects will appear. In the work of Peters[12], within the limit of small strains and curvatures, the burning velocity can be written as:

$$s_L = s_L^0 - s_L^0 \mathcal{L}\kappa - \mathcal{L}S \tag{2.4}$$

where $\mathcal{L}$ is the Markstein length, κ the curvature and S the strain rate. $\mathcal{L}$ is proportional to the laminar flame thickness. Its expression and detailed derivation process can be found in the work of Clavin et al. [31]. When Le equals unity, i.e. thermal diffusivity and molecular diffusivity balance each other, if the flame is curved convexly with respect to the unburnt mixture side, the flame speeds decreases. For $Le < 1$, with the growth of curvature flame instabilities increase. If $Le > 1$, curvature avoids the formation of cusps in the flame front and therefore tends to stable the flame front. For the sake of brevity, effects of curvature on the laminar burning velocities will not be discussed in detail in this work, cf. Linse[32].

2.2 Turbulent flame propagation

When a turbulent flow field is superimposed to the combustion process, the flame characteristics will be changed significantly. The interaction of turbulent eddies with flame fronts makes the study of turbulent combustion phenomena considerably complicated compared to the investigation of the laminar combustion. Under this condition, combustion models that based on the assumption of the scale separation (the turbulent mixing process in the inertial range is independent of chemistry) need further discussion about their application area. In this section, the derivation of typical regime diagram of the premixed turbulent combustion and characteristics of different regions in this diagram are presented, in order to provide an overview of the physics of turbulent flame propagation.

2.2.1 Derivation of the regime diagram

The definition of turbulent Reynolds number is:

$$Re = \frac{v'\ell}{s_L \ell_F} \tag{2.5}$$

where ℓ is the integral length scale. It is the length of eddies that contain most of the kinetic energy. v' is the turbulent intensity and represents the root-mean-square velocity fluctuation. It is the turnover velocity of integral scale eddies. The integral time scale can then be written as

$$\tau = \frac{\ell}{v'} \tag{2.6}$$

η is the Kolmogorov length scale. It describes the smallest turbulent eddies[33].

Through dimensional analysis it is written as

$$\eta = \left(\frac{\upsilon^3}{\varepsilon}\right)^{0.25} \tag{2.7}$$

where υ is the eddy viscosity and ε the viscous dissipation rate. Correspondingly the Kolmogorov time is defined as

$$t_\eta = \left(\frac{\upsilon}{\varepsilon}\right)^{0.5} \tag{2.8}$$

Figure 2-4 shows the location of η and ℓ in a turbulence flow field.

The Karlovitz number measures the ratio of flame scales in terms of Kolmogorov scales with the following definition:

$$Ka = \frac{t_F}{t_\eta} = \frac{\ell_F^2}{\eta^2} = \frac{v_n^2}{s_L^2} \tag{2.9}$$

It is easy to find out that the relation between Reynolds number, Damköhler number and Karlovitz number, i.e.:

$$Re = Da^2 Ka^2 \tag{2.10}$$

Here the isotropic scalar dissipation assumption is applied.

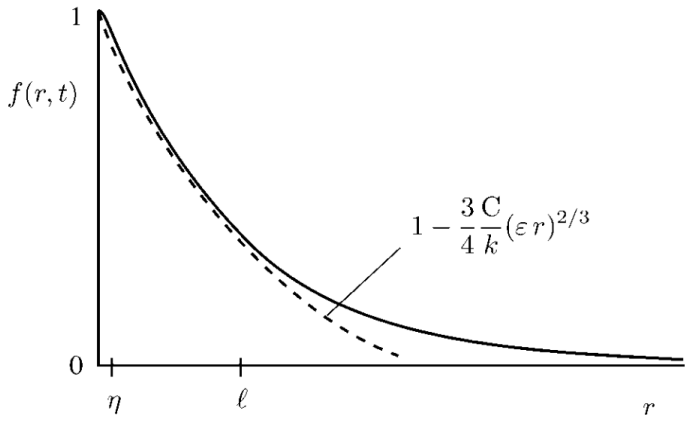

Figure 2-4 The normalized velocity correlation for isotropic homogeneous turbulent flow field[12]

Another important parameter for the turbulent premixed combustion is the thickness of the inner layer (ℓ_δ), which is obtained by the flame structure analysis, cf. Figure 2-1. A typical flame structure is illustrated in Figure 2-1. As mentioned before, the Kolmogorov length is the smallest eddies, the requirement of scale separation between turbulence and chemistry is then written as

$$\ell_\delta < \eta \tag{2.11}$$

Another Karlovitz number definition is based on these two parameters:

$$Ka_\delta = \frac{\ell_\delta^2}{\eta^2} \tag{2.12}$$

After giving all these definitions, one can obtain the following diagram for premixed turbulent combustion.

2.2.2 Regime diagram for premixed turbulent combustion

Figure 2-5 is the regime diagram for turbulent premixed combustion according to Peters[12]. The combustion region can be subdivided into five regions:

1) Laminar flames regime: $Re < 1$. The combustion process is laminar. Turbulence has no influence on the flame propagation.
2) Wrinkled flamelets regime: $Re > 1, \frac{v'}{s_L} < 1$. The turnover velocity of the integral scale eddies v' is smaller compared to the flame front propagation speed s_L. The laminar combustion is dominant and no significant interaction of turbulence with combustion appears.
3) Corrugated flamelets regime: $Re > 1, \frac{v'}{s_L} > 1, Ka < 1$. Turbulent eddies are strongly interacting with the flame front, but the smallest eddies with the Kolmogorov length η can still not enter the preheat zone. The inner layer of the flame structure keeps laminar.
4) Thin reaction zones regime: $Re > 1, Ka > 1, Ka_\delta < 1$. The smallest eddies of the Kolmogorov length η can penetrate into the preheat zone. But the inner layer is not influenced by turbulences and remains laminar.
5) Broken reaction zones regime: $Re > 1, Ka_\delta > 1$. The smallest eddies of Kolmogorov length η is of the order of the thickness of inner layer or even smaller. Turbulence strongly affect the structure of inner layer. No laminar flame structure exists.

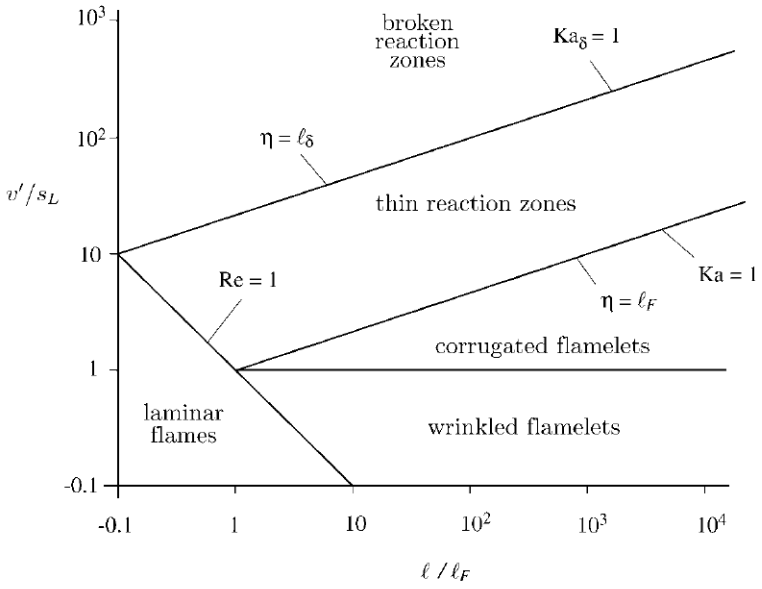

Figure 2-5 Regime diagram for turbulent premixed combustion[12]

Since what we want to investigate is the turbulent combustion, the laminar flame regime will not be considered. The wrinkled flamelets regime will not be discussed because it is not much of practical interest. The broken reaction zones regime is related to flame quenching and extinction. In this regime, a premixed flame is unable to survive. Therefore, this regime will not be discussed in the scope of this work.

For the corrugated flamelets regime, $Ka < 1$ indicates that the flame thickness is smaller than the Kolmogorov length scale, i.e. $\ell_F < \eta$, which means that the turbulence eddies cannot penetrate into the flame structure. Therefore, the flame structure remains quasi-steady. There is a kinematic interaction between the advancing laminar flame and turbulent eddies.

In the thin reaction zones regime, $Ka > 1$, i.e. $\ell_F > \eta$, indicates that the smallest turbulent eddies can enter into the flame structure. But they cannot penetrate into the inner layer because $Ka_\delta < 1$, which means $\ell_\delta < \eta$.

Since these two regimes have different characteristics, different formulations or correlations for these two regimes can be seen in lots of papers. For instance, Buckmaster et al.[34] investigated the curvature and strain on quasi-steady laminar flames. Chakraborty et al.[35] compared the displacement speed of turbulent flames in both corrugated flamelets and thin reaction zones regime. Sankaran et al.[36] analyzed the structure of premixed turbulent flames in the thin reaction zones regime by applying the Large Eddy Simulation (LES). From his simulation results one can obtain, that the thickness of the preheat zone of the flame increases with the Karlovitz number in the thin reaction zones regime. Pitsch[37] employed the LES approach and applied a filtering procedure to derive the equation. A new line that separates the thin reaction zones regime into two parts is given, where the flame thickness is smaller and larger than the filter size. Nada et al.[38] conducted the Direct Numerical Simulations(DNS) to investigate the hydrogen-air premixed flames. According to the simulation results, the heat release rate in the corrugated flamelets regime increases

up to 1.2 times of that in laminar flames, which is caused by the penetration of the coherent fine scale eddies into the flame and leads to the handgrip structure. de Goey et at.[39] analyzed the turbulent flame thickness in the thin reaction zones regime experimentally and numerically. Through the Rayleigh images one can see, that the flame front thickness becomes thinner under lean mixtures and rich mixture results in thicker flames. This is explained by investigating the influences of stretch and preferential diffusion. Chakraborty et al.[40] carried out DNS simulations to study the effects of the stretch rate on premixed flames in the thin reaction zones regime. The non-linear correlation of the flame displacement speed to the stretch rate using a simplified chemistry mechanism is consistent with the one using a detailed chemistry mechanism.

2.3 Closing remarks

In this chapter, the physics of the laminar flame propagation and turbulent combustion processes were presented. A general overview of premixed combustion phenomena built a foundation for the following part.

At first, the laminar flame structure was described and was subdivided into three distinct regions: the preheat zone, the inner layer and the oxidation layer. The thickness of the preheat zone and the inner layer are important when the turbulent flow field is superimposed in the combustion process. The inner layer is of great importance for the combustion process, since the rate-determining reactions occur in this layer. If the reactions in this layer break down, flame extinguishing might appear.

Another important characteristic length scale is the thickness of the laminar flame ℓ_F. It is proportional to the laminar burning velocity s_L. Therefore, the accurate measured s_L is a necessary prerequisite for the evaluation of ℓ_F. Different experiments were carried out and the influencing factors on the s_L were discussed. The effects of curvature and strain on a three-dimensional propagating flame were briefly mentioned.

The second section focused on the famous regime diagram for the premixed turbulent combustion. The different parameters and numbers used to distinguish different regions were defined and explained. Five different conditions in premixed turbulent flames: laminar flamelets regime, wrinkled flamelets regime, corrugated flamelets regime, thin reaction zones regime and the broken reaction zones regime. Characteristics of the combustion phenomena in these five regimes were analyzed. For the interest of this work, in the following part, the corrugated flamelets regime and the thin reaction zones regime will be discussed in detail.

3 Turbulent Combustion Models

Turbulent combustion is a broad area of research. Lots of work has been devoted to combustion modeling. For premixed turbulent combustion, there are several models being proposed and widely used. In terms of chemistry rate being applied, the most widely used models can be classified as in Table 3-1. This section provides an overview of the combustion models mentioned in Table 3-1 and introduces basic concepts used in modeling the interaction of turbulence and combustion.

Table 3-1 Classification of turbulent premixed combustion models in terms of chemistry mechanism

Infinitely fast chemistry	Coherent Flame Model
	Bray-Moss-Libby Model
Finite rate chemistry	PDF Transport Equation Model
	Linear Eddy Model
	Flamelet Model

3.1 Coherent Flame Model (CFM Model)

Coherent Flame Model (CFM)[41] uses infinitely fast chemistry assumption and is classified to the category of flame surface models. The time determining time scale is the integral time, which was defined in equation 2.6. The flame thickness is smaller than the integral length scale.

A flame sheet divides the flow field into two parts, reactants and combustion products existing on each side of the sheet. The turbulence distorts this flame sheet extensively. All chemical reactions take place within a region which is small compared to the predominant length describing the distortion of the flame front[41]. CFM model was employed in a series of papers to predict the flame propagation in SI engines.

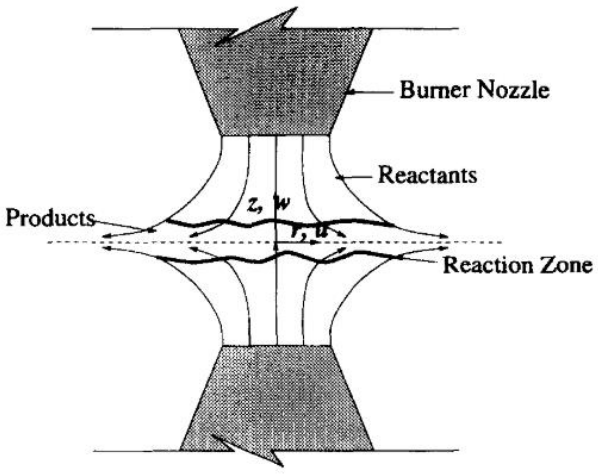

Figure 3-1 Premixed turbulent combustion in a counterflow geometry[42]

A field variable that specifies the flame surface area is defined as

$$\Sigma(x_i, t) \tag{3.1}$$

and was described by non-linear equations. All equations contain a turbulent diffusion term. Gu et al.[42] utilized a counterflow burner (Figure 3-1) to validate the CFM model. The model constant β was selected for the model, in order to get good agreement between numerical and experimental results.

In order to predict the laminar flame kernel radius at the early flame propagation phase, Boudier et al.[43] added a laminar flame ignition model as a complement of the existing model. A modified ε-equation is applied to model the transition process from laminar to fully turbulent combustion. Duclos et al.[44] used this model to study the pollutant formation in a stratified charge SI engine. Since the CFM model is based on the infinitely fast chemistry, a finite chemistry is applied in order to predict the concentrations of NO and CO. An Extended Coherent Flame Model (ECFM) is derived by Duclos et al.[45]. Through the experimental data of Mitusbishi DI-SI engine the prediction ability of this model is validated. Bougrine et al.[46] studied the heat release, pollutants formation and knock phenomena of an ethanol blended gasoline SI engine. New formulated laminar flame speed and knock delay correlations and modified chemical reactions in flame fronts are adopted to get good agreement with the experiment data.

3.2 Bray-Moss-Libby Model (BML Model)

Bray-Moss-Libby model is another classical model for the premixed turbulent combustion. It is initiated by Bray and Moss[47]. Fast chemistry assumption and single step global reaction are used to derive the balance equation. It introduces the progress variable c as a scalar quantity and assumes the Probability Density Function (PDF) of the progress variable to be a double delta-function distribution. In the model c is viewed as a normalized temperature:

$$c = \frac{T - T_u}{T_b - T_u} \tag{3.2}$$

where the subscripts u and b indicate the unburnt and burnt state.

The Favre-averaged transport equation of the mean progress variable $\tilde{c}$ can be written as

$$\frac{\partial(\bar{\rho}\tilde{c})}{\partial t} + \frac{\partial(\bar{\rho}u_i\tilde{c})}{\partial x_i} = -\frac{\partial\left(\bar{\rho}\widetilde{u_i''c''}\right)}{\partial x_i} + \overline{\dot{\omega}_c} \tag{3.3}$$

The first term on the right-hand side of equation 3.3 is the turbulent flux term. The second term is the chemical source term. Both of them need to be closed. Generally, the scalar flux term is closed using a gradient diffusion assumption and the chemical reaction rate is modeled by the scalar dissipation rate.

Bray et al.[48] also developed a Reynolds stress/flux description for a steady flow field. Gradient transport and counter-gradient transport are also investigated. For finite chemistry, Bray and Champion[49] investigated the effects of the presumed PDF on the prediction of the mean reaction rate. Among three chosen PDF functions, the two delta-function and the beta function lead to significant errors, while the PDF based on the unstrained laminar flame property has a favorable agreement with the DNS. Furthermore, Schneider et al.[50] validated the potential of BML model for partially premixed flames. In order to account for the interaction between chemistry and

turbulence, a presumed PDF approach is used.
However, the assumption used to close the turbulent flux term is in general not valid for reactive flows. It could lead to unphysical counter-gradient transport which should be avoided.

3.3 PDF Transport Equation Model

In turbulent flow fields, scalars such as temperature, velocity, mass fraction and pressure are instantaneously fluctuating and stochastic quantities. PDF plays a significant role in theoretical analysis of turbulent flows. It gives a general statistical description of turbulent fields and flows. A complete statistical description of a single point in the flow fields is achieved by the joint PDF of velocity and other reactive scalars. Since gradients of velocity and other reactive scalars can be included in the equation, they could provide information at neighboring points. Therefore, viscous and scalar dissipation modeling become possible[12]. The detailed derivation process of the balance equation for the joint PDF of velocity and reactive scalars can be found in Pope[51]. The equation reads

$$\frac{\partial(\rho P)}{\partial t} + \nabla\cdot(\rho \boldsymbol{v} P) - \nabla\bar{\rho}\cdot\nabla_{\boldsymbol{v}} P + \sum_{i=1}^{N}\frac{\partial}{\partial\psi_i}(\omega_i P)$$

$$= \nabla_{\boldsymbol{v}}\cdot(-\langle\nabla\cdot\tau|\boldsymbol{v},\psi\rangle + \langle\nabla p'|\boldsymbol{v},\psi\rangle - \sum_{i=1}^{N}\frac{\partial}{\partial\psi_i}(\langle\nabla\cdot(\rho D\nabla\psi_i|\boldsymbol{v},\psi\rangle P) \qquad (3.4)$$

Two terms on the right-hand side of the equation are unclosed and need to be modeled. The most challenging term, the chemical source term ω_i appears in closed form. Janicka et al.[52] derived the PDF transport equation of a scalar variable in turbulent field. This transport equation is closed by various closure approximations. Baldwin et al. [53] got a one-equation turbulence model deriving from a simplified $k-\varepsilon$ standard model equations. The simulation results of a flat plate flame showed that the model has predictive properties comparing with experimental data. Pope[54] provided a complete statistical description of the flow field state using the velocity composition joint PDF. The equation derived does not include scalar gradients, which indicates that this model does not contain the information like the mixing time. Girimaji et al.[55] validated and extended the prediction ability of the model by applying a β-PDF function for the case of two to multiple turbulent scalars mixing. The joint PDF of the scalar concentrations related to mean scalar concentrations and turbulent scalar energy.
Since the chemical source term in the balance equation is closed and does not need to be modeled, it is often argued that the PDF transport equation model is better than other methods. But the very high CPU demand when the detailed chemical mechanism is integrated in the model is a major drawback of this method. Furthermore, the application of the scale separation assumption to the combustion processes that occur in thin reaction zones regime is questionable, because eddies with the size of the Kolmogorov length can enter to the flame layer.

3.4 Linear Eddy Model (LEM Model)

Linear Eddy Model (LEM) is the only model without assuming the scale separation. Since this model does not specify the choice of the turbulent mixing model, it can be applied also to the non-premixed combustion simulation just like the PDF transport equation model. This model proposed by Kerstein [56] describes the turbulent convection by a random sequence of scalar field rearrangements. All relevant length scales were resolved in one dimension. The rearrangement events simulate numerically scalar dissipation rate by modeling the event rate. Each rearrangement event along the line is viewed as the effect of a single eddy on the scalar field. It allows the interaction between chemistry and turbulence in the inertial range. This model has the potential to accurately describe uncommon phenomena occurring in the combustion process, such as extinction, differential diffusion and reignition[57].

Menon et al.[58] introduced an instantaneous triplet map to get one spatial representation of the turbulent advection. This strategy achieves the robust and affordable accurate prediction. The triplet map mentioned simulates the effect of an eddy turnover and obeys applicable conservation laws, which is illustrated in Figure 3-2.

This model contains a process that describes the evolution of the reactive scalar field. The governing equation is

$$\frac{\partial(\rho\psi_i)}{\partial t} = \frac{\partial}{\partial x}\left(\rho D_i \frac{\partial \psi_i}{\partial x}\right) + \omega_i \tag{3.5}$$

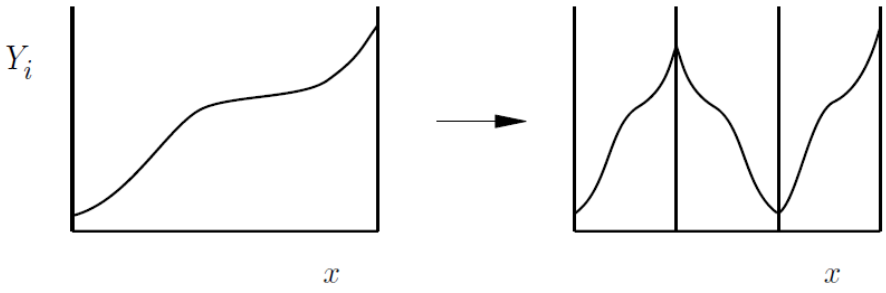

Figure 3-2 Illustration of a triplet map used in the Linear Eddy Model accounting for the rearrangement event due to turbulent mixing[12]

Menon et al.[59] integrated the LEM formulations to the large eddy simulation (LES) and employed it to simulate the combustion process in a shear layer. The simulation results were compared with the experimental data and the good agreement was found. Smith et al.[60] investigated the freely propagating premixed turbulent flames based on this model. Similar trends of the turbulent burning velocity s_T were obtained by comparing with the DNS data, when Lewis number varied from 0.8 to 1.2. The recent application of this model on non-premixed combustion can be found in Sankaran et at.[57] ‘s work. They developed a tabulated closure for non-premixed flames using the Linear Eddy Model (LEM). The conditional statistics extracted from the tabulated LEM

data matched the measured ones well. The local extinction phenomenon was captured.

3.5 Flamelet Model based on the G-Equation

The flamelet concept was derived by considering, that the integral time scale is bigger than the chemical time scale, i.e. chemical reactions take place relatively fast in comparison to the turbulence characteristic time scale. In the work of Peters[13], he pointed out, that this situation occurs in most practical combustion systems in engineering applications including reciprocating ICEs. Premixed flamelets extinguish principally not as easily as diffusion flamelets, because they are embedded between the hot burnt gas and the cold unburnt gas, instead of between two cold mixtures.

The inner structure of the flamelets is time-dependent and one-dimensional. Their location depends on the flow field and is determined by the interaction of the flame with the entire range of length and time scales of the oncoming flow. A typical structure of the flamelets is depicted in Figure 2-1 in chapter 2, cf. Peters[13] where a reduced four-step mechanism was used.

Flamelets are thin reactive-diffusive layers where the chemical reactions occur. Therefore, the turbulent flame can be viewed as a combination of stretched laminar layers and the combustion process can then be separated from the turbulent flow. A detailed derivation of the flamelet equations is given by Peters[12]. The flame stretch effect increases the scalar dissipation rate in a turbulent flow field. If it exceeds a critical value the diffusion flamelet will extinguish. Furthermore, local extinction events may interrupt the connection to burnable flamelets which are not yet reached by an ignition source and will therefore not be ignited.

Other than methods that are based on a PDF transport equation, the key issue in flamelet models is the accurate estimation of the probability of finding the flame front at a given position x and time t. As long as the flame front position is determined, one can attach the 1D profile of reactive scalars along the normal direction of the flame front surface.

One of such flamelet models for the premixed turbulent combustion is proposed by Peters[12] and is known as the G-equation model. The scalar G is a non-reacting quantity, which is different from BML model and CFM model (In these two models, the reactive scalar was chosen in the controlling equation) mentioned before. The model used in this work is exactly the G-Equation based Flamelet Model. The detailed derivation process and the application examples of this model are given in chapter 4.

Cook et al.[61] applied laminar flamelet concept to LES and extended a subgrid-scale model for the equilibrium chemistry to include the finite-rate chemistry. The accuracy of the model was validated by the data sets from DNS. Mittal et al.[10] used the Representative Interactive Flamelet （RIF） model to account for concurrent thermal and charge stratifications in diesel engines.

3.6 Closing remarks

In this chapter, five combustion models used for premixed turbulent combustion investigations were presented. Except for PDF transport equation models and LEM

method, other models employ the assumption of scale separation.

Flamelet models employ conserved scalars that account for chemistry by providing state relationships for the reactive scalars. The biggest challenge for reacting flows is that the appearance of unclosed chemical source terms. For flamelet models that are based on the reacting scalars, the appearance of the unclosed chemical source term in the balance equation is unavoidable. The BML model and CFL model suffer from this fact. It is challenging to find an appropriate closure for this chemical source term.

PDF methods either presume the shape or solve a transport equation for the joint PDFs to characterize the interactions of scales. Chemical source terms appear in closed form within the transport equation regardless of the regimes of combustion process.

A combustion model that can avoid the appearance of unclosed chemical term, accurately estimate the position of the flame front surface and the corresponding heat release is the G-equation based flamelet model. The scalar G is non-reacting, which was proposed by Peters[12].

Although the first four models mentioned in this chapter could provide reasonable simulation results that get good agreements with measured data or with DNS results, the occurrence of the counter-gradient diffusion during the combustion process must be dealt specifically. Other assumptions and modified constants in the equation should be employed to get reasonable results, which sometimes lack physical meaning or violate the physical laws. Another tough term in the equations that is very difficult to model is the source term. As long as a reactive scalar is chosen, the appearance of this term in the equations is unavoidable. On the contrary, the flamelet equation based on the G-equation avoid these problems. A more detailed introduction about this model is given in chapter 4.

4 Eulerian Flame Tracking Model

The Eulerian Flame Tracking Model (EFTM) is a flamelet model based on the Level Set approach (also called G-equation) for premixed turbulent flames. This model is based on the non-reacting scalar G proposed by Peters[62]. One of several advantages of this model has been mentioned at the end of chapter 3. The kinematic equation in this model was firstly derived by Williams[63] for laminar premixed flames and then extended by Peters[64] for turbulent premixed combustion areas. Due to the advantages of level set approach for tracking the evolving interfaces and the non-reacting scalar G, this model is especially suitable for engineering applications.

4.1 Level Set Approach

The level set approach is proposed by Osher et al.[65] and Sethian[66]. It is a numerical technique for tracking the dynamic surfaces, which is very suitable for implicit geometries. It has been widely used in recent years for tracking, modeling, and simulating the evolution of the interfaces including e.g. imaging processing, CFD and many others. This method relies on two main embeddings:

1) the embedding of the tracking surface as a zero-level set of a higher dimensional function;
2) the extension of the velocity of the surface to this higher dimensional level set function.

The zero iso-surface Γ in a three-dimensional domain can be defined as

$$\Gamma = \{(x, y, z) \in \mathbb{R}^3 | \, \phi(x, y, z) = 0\} \tag{4.1}$$

where $\phi(x, y, z)$ is the level set function and $\mathbb{R}^3$ the three spatial dimensions. The iso-surface $\phi(x, y, z) = 0$ represents the two-dimensional interface. $\phi(x, y, z) > 0$ is in the exterior region and $\phi(x, y, z) < 0$ in the interior region. The signed distance function was defined to be positive on the outside, negative on the inside, zero on the interface. $|\phi(x, y, z)| = 1$ is imposed[67]. A signed distance function is depicted in Figure 4-1.

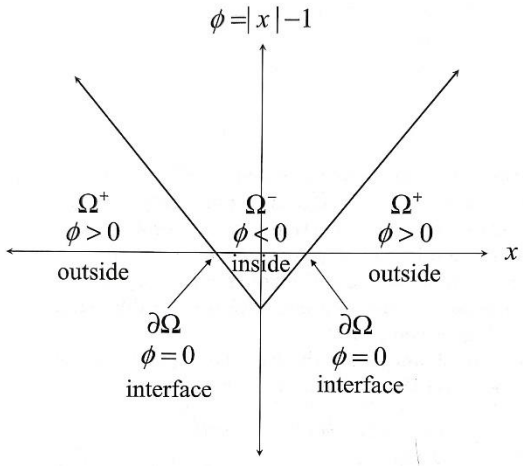

Figure 4-1 Signed distance function $\phi = |x| - 1$ defining the regions Ω^+, Ω^- and the boundary lines[67]

Assuming that the velocity of every point on the interface is known, the simplest way to move all the points in this surface with the given velocity field is to solve the ordinary differential equation (ODE)

$$\frac{d\boldsymbol{x}}{dt} = \boldsymbol{v}(\boldsymbol{x}) \tag{4.2}$$

Since the number of points on the implicit surface is usually infinite, a discretization procedure needs to be adopted, in order to get the finite number of the points in this dynamic front. This is not very difficult to achieve if the connectivity of the discretized elements does not change. However, because of the influence of the velocity field, surface elements are distorted obviously, even if the velocity changes slightly. Therefore, the discretization should be modified periodically for the desired accuracy of the method, which means the mesh-refinement procedure can account for the deformation of the surface and smooth the inaccurate surface elements.

The use of equation 4.2 for describing the evolution of the surface along with numerical techniques for smoothing, modifying and regularizing are referred as front tracking methods.

The flame front tracking is of great interest. Different from the traditional numerical algorithms employed in the flame tracking, which parameterize the moving front by several variables and then discretize this parameterization into a sequence of marker points, the level set approach deploys the implicit function both to represent the surface and to evolve the surface. Therefore, topological complexities and changes in the moving front can be handled naturally.

Correspondingly, the G-equation uses the non-reactive scalar G to represent the evolution of the flame front as an iso-surface just like the level-set approach. The level-set $G = G_0$ corresponds to the instantaneous flame front. The moving of the surface is the flame front propagation. The extension of the G-equation to the entire computational domain is performed by the transformation of the G-scalar field to a signed distance function enforcing

$$|\nabla G| = 1 \tag{4.3}$$

This is the so-called reinitialization. By using specific numerical techniques to maintain the level-set function G as a smooth distance function, gradients calculating is quite easy. The capture of curvatures appearing in the moving surface becomes straightforward. What's more, since the function G is defined everywhere and being smooth, extending the G-scalar transport to the entire computational domain is feasible, which makes it easier to implement it in the framework of AVL FIRE™.

4.2 Transport equations for mean flame front and flame brush thickness

Based on the level set approach, the kinematic equation of the mean flame front with respecting to the non-reactive scale G is written as

$$\bar{\rho}\frac{\partial \tilde{G}}{\partial t} + \bar{\rho}\tilde{\boldsymbol{v}} \cdot \nabla \tilde{G} = (\bar{\rho} s_T^0)\left|\nabla \tilde{G}\right| - \bar{\rho} D_t \tilde{\kappa}\left|\nabla \tilde{G}\right| \tag{4.4}$$

Correspondingly, the variance equation reads as

$$\bar{\rho}\frac{\partial \widetilde{G''^2}}{\partial t} + \bar{\rho}\tilde{\boldsymbol{v}}\cdot\nabla\widetilde{G''^2} = \nabla_{||}\cdot\left(\bar{\rho}D_t\nabla_{||}\widetilde{G''^2}\right) + 2\bar{\rho}D_t\left(\nabla\tilde{G}\right)^2 - \bar{\rho}c_s\frac{\tilde{\varepsilon}}{\tilde{k}}\widetilde{G''^2} \qquad (4.5)$$

Therein, G is a non-reacting scalar proposed by Peters[12] and represents the moving flame front, as shown in Figure 4-2. An equation for G was derived by considering an iso-scalar surface, namely the flame front surface,

$$G(\boldsymbol{x}, t) = G_0 \qquad (4.6)$$

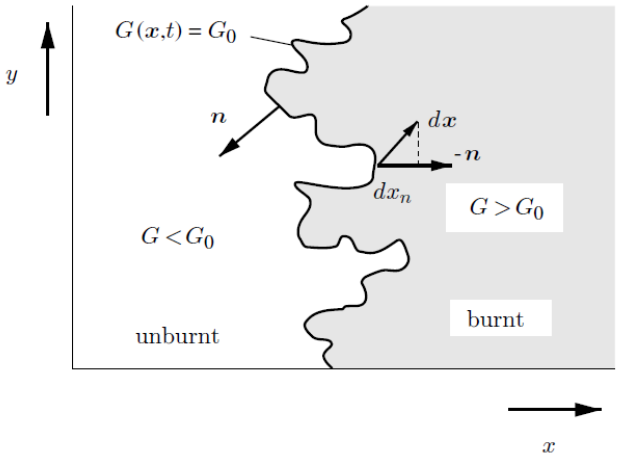

Figure 4-2 A schematic representation of the flame front as an iso-scalar surface $G(\boldsymbol{x}, t) = G_0$ [12]

According to the Figure 4-2, this surface divides the whole flow field into two parts. $G > G_0$ represents the region of burnt gas and the unburnt gas area belongs to $G < G_0$. $G''|_{G=G_0}$ is the distance between the instantaneous flame front and the mean flame front. Therefore, the turbulent flame brush thickness can be defined based on the G''.

$\boldsymbol{v}$ is the convection velocity of the flame front. s_T^0 is the unquenched turbulent flame burning velocity. $|\nabla\tilde{G}|$ is the gradient of the scalar G. D_t is the coefficient of the turbulent diffusivity of the tracked species. $\tilde{\kappa}$ is the curvature of the flame front ($\tilde{\kappa} = 0$ for a planar freely propagating flame). c_s is a model constant and is recommended to be 2 by Peters[12] (see Table 4-1). ε is the turbulent dissipation rate and $\tilde{k}$ can be viewed as the fluctuation of the turbulent velocities.

Two terms on the left-hand side of the equation 4.4 are the movement of the iso-surface, since the G scalar is a function of time and spatial location. The first term on the right-hand side of the equation 4.4, i.e. $(\bar{\rho}s_T^0)|\nabla\tilde{G}|$ describes the mass burning rate, indicates the contribution of the turbulent flame propagation to the evolution of the mean flame front. The second term accounts for the turbulent diffusivity and curvature.

For the G-variance equation, the turbulent transport is denoted by $\nabla_{||}\cdot\left(\bar{\rho}D_t\nabla_{||}\widetilde{G''^2}\right)$. The subscript || means only the tangential gradient transport is accounted for. $2\bar{\rho}D_t\left(\nabla\tilde{G}\right)^2$ represents the turbulent production term. The last term on the right-hand side of the equation 4.5 is the turbulent dissipation term.

It needs to be noted that these two equations are valid at $\tilde{G}(\boldsymbol{x}, t) = G_0$ only. For the

sake of brevity, only two key equations are given here. The detailed derivation process of these two equations can be found in the work of Peters[12] and Linse[32].

4.3 Modeling of the turbulent flame burning velocity s_T

As mentioned in section 2.1, the laminar burning velocity s_L is the most important quantity in the laminar premixed combustion. Correspondingly, in the turbulent premixed combustion area, determining the turbulent burning velocity s_T is also the cornerstone of the accurate combustion model. In order to clarify the influencing factors on the turbulent burning velocity and determine s_T experimentally, Bradley et.al [68] carried out a series of experiments with a combustion vessel. Kobayashi et.al[69] explored the effects of ambient pressures on the turbulent burning velocity with a nozzle-type Bunsen burner. Premixed flames of lean methane-air mixtures were investigated experimentally up to 3.0 MPa. Based on the conclusions extracting form the work of lots of researchers, the turbulent burning velocity depends directly on the laminar flame burning velocity s_L, turbulence intensity v' and the integral length scale ℓ for a given fuel-air mixture[12]. The existing correlations for s_T can be found in various combustion literatures. Two different kinds of velocity model were applied in this master thesis, i.e. the Ewald velocity model and the G-equation based Flame-Wall Interaction model (GFWI model). A detailed explanation of these two models is given in this section.

4.3.1 Ewald model

The modeling of s_T proposed by Ewald[70] is subdivided into two models, i.e. the spark ignition model and the unsteady premixed combustion model.
For the unsteady premixed combustion model, the correlation of s_T with s_L is defined as

$$s_T = (1 + \widetilde{\sigma_t}) \cdot s_L \tag{4.7}$$

Therein, $\tilde{\sigma}$ is the turbulent flame surface area ratio and reads as

$$\widetilde{\sigma_t} = \frac{A_T}{A} \tag{4.8}$$

where A_T is the instantaneous flame surface area and A is the cross-sectional area. Figure 4-3 shows their relation schematically. Since the laminar burning velocity s_L is a well-defined parameter and can be measured via experiment. The prerequisite for the calculation of s_T is the determining of the turbulent flame surface area ratio.
$\widetilde{\sigma_t}$ is modeled using the following correlation:

$$\widetilde{\sigma_t} = \frac{\ell_{F,t}}{\ell_F}\left(-\frac{b_3^2}{4b_1}\sqrt{\frac{3c_\mu c_s}{Sc_t}} + \sqrt{\frac{b_3^4}{16b_1^2}\frac{3c_\mu c_s}{Sc_t} + \frac{c_s b_3^2}{2}\frac{\ell_F}{s_L}\frac{\varepsilon}{k}}\right) \tag{4.9}$$

Equation 4.9 established relationship between the ratio of flame front thickness and the turbulent flame front surface area ratio. The turbulent flame front thickness $\ell_{F,t}$ based on the G-equations can be written as

$$\ell_{F,t} = \frac{\sqrt{\widetilde{G''^2}}}{|\nabla \tilde{G}|} \tag{4.10}$$

Two terms in parentheses rely on the turbulent time scale and laminar flamelet properties. Constants appearing in equation 4.9 is summarized in Table 4-1.

Table 4-1 Model constants of $\widetilde{\sigma_t}$-equation

Constant	Suggested Value	Reference
b_1	2.0	Abdel-Gayed[71]
b_3	1.0	Damköhler[72]
c_s	2.0	Peters[64]
Sc_t	0.7	Ewald[73]
c_μ	0.089	Ewald[73]

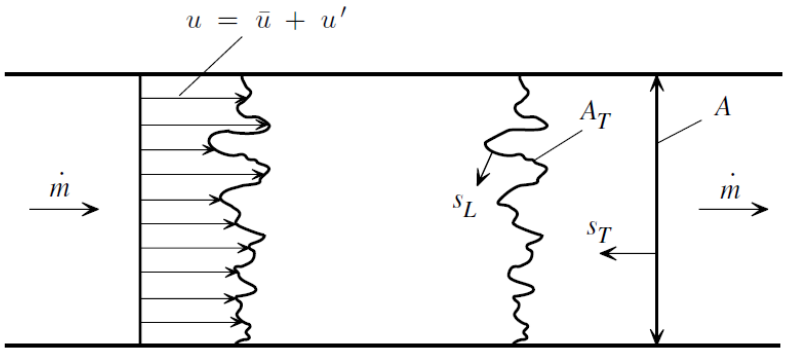

Figure 4-3 A schematic description of the steady flame propagation in a duct[12]

Different from the assumptions for the premixed turbulent flame propagation model, the kernel expansion effects caused by the electrical energy discharge and the kernel curvature effects should also be considered. Therefore, an ignition model was also proposed by Ewald to estimate the flame kernel formation and the early stage of the flame front propagations.

Two important assumptions for the modeling set-up are:

1) The initial spark kernel is spherical with a given initial radius at the specific location;
2) The kernel is subjected to the convection of the background flow before it reaches a specific size r_c. (r_c is the radius where the combustion switches from the spark model to the combustion model).

$s_{T,k}$ is written as

$$s_{T,k} = s_T - \kappa D_t' = s_T - \frac{2}{r_K} D_t^{'} \tag{4.11}$$

where r_K is the radius of the flame kernel. $D_t^{'}$ is modeled by the following equation

$$D_t^{'} = \sqrt{\frac{c_\mu c_s}{2Sc_t}} \ell_{F,t} k^{0.5} \tag{4.12}$$

Using the asymptotic analysis and the assumption of uniform turbulent profiles, one can get the equation describing the flame brush thickness like $\widetilde{G''^2}$-equation:

$$\frac{d\widetilde{G''^2_{spk}}}{dt} = 2\widehat{D}_{t,spk} - c_s \frac{\varepsilon}{\hat{k}_{spk}} \widetilde{G''^2_{spk}} \tag{4.13}$$

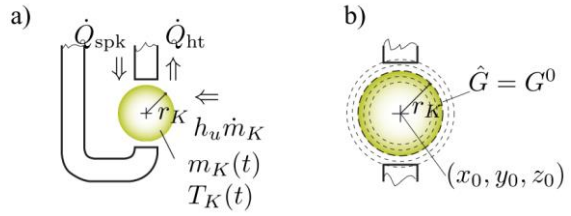

Figure 4-4 a) Energy balance between the flame kernel and the spark plug electrodes b) connection between G-field and the flame kernel[74]

For SI engines, the initial condition is $\widetilde{G''^2} = \widetilde{G''^2_{spk}} = 0$. When the flame kernel reaches an artificially set critical size r_c, the model is switched to the premixed turbulent combustion model.

This velocity model overcomes problems when the flame thickness becomes small in comparison to the numerical grid used in the simulation, since the turbulent burning velocity s_T is the model input.

4.3.2 GFWI model

Suckart and Linse[75] extended the Ewald velocity model by taking the flame quenching phenomena and near wall turbulence effects into account. The cornerstone of the new turbulent burning velocity is, only the unquenched flamelets contribute to the whole flame front propagation. They assumed that each single flamelet can only have two states, i.e. unquenched and quenched. The transition process is neglectable. The unquenched factor Q is therefore defined as (proposed by Suckart and Linse[75]) :

$$Q = \mathrm{erf}\left(\frac{x_Q}{\sqrt{2\ell_{F,t}^2}}\right) \tag{4.14}$$

where x_Q is the distance of the mean flame front to the wall subtracting the length of the quenching zone (their relation is depicted in Figure 4-5) and is written as

$$x_Q = x_w - y_Q \tag{4.15}$$

$\ell_{F,t}$ is consistent with the definition given in equation 4.10.

The quenched turbulent burning velocity is written as

$$s_{T,Q} = Q \cdot s_T \tag{4.16}$$

s_T is determined by the unquenched laminar burning velocity s_L and the turbulent flame surface area ratio

$$s_T = s_L(1 + \bar{\sigma}_t) \tag{4.17}$$

$\bar{\sigma}_t$ is closed by

$$\bar{\sigma}_t = -\frac{c_t b_3^2}{2b_1}\frac{\ell_{F,t}}{\ell_F} l^{*\frac{5}{3}} + \sqrt{\left(\frac{c_t b_3^2}{2b_1}\frac{\ell_{F,t}}{\ell_F} l^{*\frac{5}{3}}\right)^2 + c_t b_3^2 l^{*2}\frac{v'}{s_L}\frac{\ell_{F,t}}{\ell_F}} \tag{4.18}$$

The modeling constant c_t is suggested to be 1.91ζ by Suckart[75] when the turbulent model $k-\zeta-f$ was used.
The scaling factor l^* is defined as

$$l^* = \frac{\ell_{F,t}}{\ell_F}\left(\frac{3c_t}{0.37c(Q)}\right)^{-0.5} \tag{4.19}$$

For the sake of brevity, only the essence of the formulations for s_T is discussed here. For detailed derivation process, cf. Suckart and Linse's work[75].

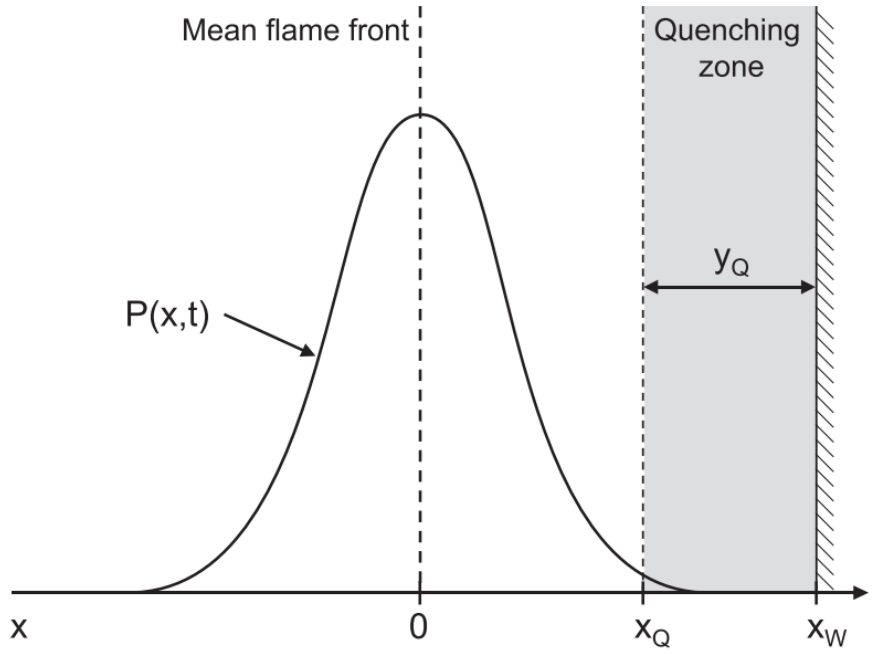

Figure 4-5 A one-dimensional premixed turbulent flame interacting with a wall[75]

According to the simulation results, the impact of the quenching distance y_Q on the quenching factor Q is neglectable. Thereby, y_Q is kept as a model constant in the simulation processes and equals $50\mu\mathrm{m}$. The turbulent burning velocity decreases when the flame front propagates near the wall $(y^+ < 50)$. This flame-wall interaction was considered by introducing the quenching factor Q as a scaling factor in equation 4.16.

4.4 Applications of the G-equation model to SI engines

After Peters proposed the non-reactive scalar G, Kellner -Sornig[76] firstly applied the G-equation based premixed turbulent combustion model to the SI engine. The mean flame front position $\tilde{G}$-equation, the flame brush thickness G''-equation and the flame surface area ratio $\bar{\sigma}$-equation were solved in his dissertation. This showed the potential of the level set approach for modeling turbulent combustion processes in actual engines.
Afterwards, Dekena[77] employed the G-equation model to simulate the turbulent flame propagation process in a DISI engine. Different from Sornig's work, he used an algebraic correlation for the turbulent burning velocity instead of solving the $\bar{\sigma}$-equation. Ewald et al.[70] extended the model via a linear correlation between the turbulent flame brush thickness and the turbulent burning velocity so that this model

can consistently simulate the evolution of the premixted flame from laminar into fully developed turbulent flames, as discussed in section 4.3.1.

The spark ignition model discussed in section 4.3.1 was based on the work of Tan et al.[78]. During the initial ignition process, the ignition kernel is assumed to be spherical and the growth rate of kernel is highly influenced by the spark discharge energy. Once the ignition kernel exceeds a critical radius, the flame can be thought of as a fully developed turbulent flame. The ignition model switches to the combustion model and effects of flow turbulences on the kernel growth rate become dominent. The critical flame kernel radius r_c, which determines the model switching, is chosed arbitrary.

In order to clarify the influences of the chemical mechanisms on the simulation accuracy of the combustion process, Liang et at.[79] linked a 100-species, 539-reactions propane detailed mechanism and a reduced 9-reactions NO_X formation mechanism to the G-equation based combustion model. A homogenous charge SI engine with the C_3H_8 as the fuel was used to validate the model. The predicted results matched the experimental data very well. A stratified charge DISI engine with the gasoline as the fuel was also investigated. A 21-species, 42-reactions isooctane iC_8H_{18} mechanism was used. Good agreement with measured in-cylinder pressures and NO_X formation for a wide range of operating conditions was obtained.

Different from the work of Suckart and Linse[75], Yang et al.[80] empoyed the G-equation model to simulate the flame front quenching phenomenen in highly stratified mixtures which are typical in late-injected gasoline DISI engines. The effects of local residual gas levels on the turbulent burning velocity was also considered. The simulation results on a gasoline turbocharged DI engine showed that the computational in-cylinder pressure, heat release rate and burned masss fraction agreed with the measured data considerably well.

4.5 Closing remarks

In this chapter, the G-eqation based EFTM combustion model is detailed discussed and the application cases of the level set approach are presented.

The flamelet concept is based on the assumption of the scale seperation. It postulated that the flame is infinitely thin and that even the smallest turbulent eddies can not penetrate into the flame. This kind of premixed flame belongs to the regime of corrugated flamlets. However, according to Linse et al.[81] ‘s research the combustion process often takes place in the thin reaction zones regime in turbocharged DISI engines. As a result, a combustion model should also be valid in this regime. The EFTM model is the one that meets this requirement. The EFTM combusition model is based on the G-equation. Through various application cases of the G-equation by other researchers shown in part 4.4, the prediction ability of this model is validated.

In the G-equation based EFTM model, the turbulent flame front tracking is achieved by the level set approach, which is identified by the isosurface $G = G_0$. This model has following considerable advantages compared to other models:

1. Since the scalar G is a non-reacting quantity, it avoids the appearance of the source term in controlling equations and the countergradient transport.
2. The G-equation model is derived seperately for the corregated flamelet regime and

the thin reaction zones regime. Through the scale analysis a general form is formulated.

3. Due to the kinematic level set approach employed, the turbulent burning velocity s_T is the model input into the kinematic equation and not a reaction rate defined per unit volume. This approach therefore overcomes problems in case that the (laminar or turbulent) flame thickness becomes small in comparison to the numerical grid used in the problem simulation and in that limit, the reaction rate would become a delta peak, wich is difficult to be integrated numerically.
4. By combining the G-equation with flamelet equations, the integration of detailed chemical mechanisms to the model is possible.
5. Through the application examples by losts of researchers it is clear that the G-equation can be applied to premixed and partially premixed combustion.

5 Model Validation

After implementing the EFTM into AVL FIRE™, various cases were used to validate this G-equation based model. Simple and academic cases were carried out to evaluate the numerical implementation of the model. Afterwards, the laminar combustion process in a combustion bomb was investigated. Finally, in order to assess the accuracy and robustness of the G-equation model under practical conditions, the flame propagation process in a pancake engine with the flat cylinder head and flat pistion and in a single-cylinder AVL prototype DISI engine with detailed geometry structures were modeled. The simulation results were compared with the experimental pressure histories and high speed Schlieren imaging data.

5.1 Numerical Studies

5.1.1 Propagating spherical Front

In this numerical case, a sphere with an initial radius of $r_0 = 3\,mm$ propagates through a quiescent fluid field. By ignoring the curvature term and generating a zero external velocity field, the equation 4.4 reduces to

$$\frac{\partial \tilde{G}}{\partial t} = s_T \left|\nabla \tilde{G}\right| \tag{5.1}$$

The computational domain was a cube discretized by a structured hexahedron mesh. In order to evaluate the sensitivity of the numerical scheme to the cell size and the time step, two different 3D meshes and different time steps were used. The mesh information is summarized in Table 5-1 and depicted in Figure 5-1.

Table 5-1 Propagating sphere front in a cube - mesh hierarchy

Mesh	Cell length	Cell numbers
Cube_1	1mm	64000
Cube_2	0.5mm	512000

The results for the time step sensitivity analysis are plotted in Figure 5-2 and Figure 5-3. Figure 5-2 shows that the mean reaction progress variable using the time step $\Delta t = 0.01\,ms$ matches the one using the time step $\Delta t = 0.005\,ms$ very well. At the early stage of the flame front propagation, two lines overlap with each other. The difference increases with the time. This is probably due to the increasing CFL number. The definition of the CFL number is as below:

$$CFL = s_T \frac{\Delta t}{\Delta L} \tag{5.2}$$

where ΔL is the cell length. Since the turbulent burning velocity increases with time, the CFL number of the case, that uses a bigger time step, increases faster, which leads to a bigger error (the same cell size has been adopted). For the refined mesh Cube_2, the same trend can be found in Figure 5-3.

Figure 5-4 shows the mean reaction progress variable of two meshes with the same time step. At the early stage of the flame propagation process, two lines overlap and the very good agreement can be obtained. The slight difference at the end of the

combustion is mainly due to the G-equation solving process. The same flame front area should be solved more times in the refined mesh Cube_2, since the number of cells that contain the flame front surface is much more than the Cube_1. Furthermore, as the flame front propagates, the number of cells keeps increasing. However, when compared to the overall time range, this slight difference could be neglected.

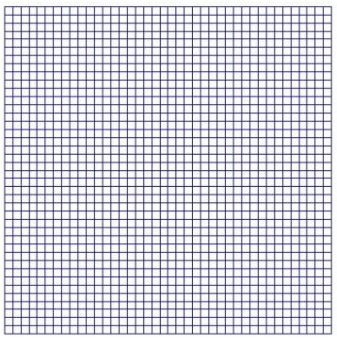

Figure 5-1 Mesh of the propagating sphere test case

The results show that the overall accuracy is very good even for big CFL numbers. For smaller CFL numbers only more accurate results are obtained.

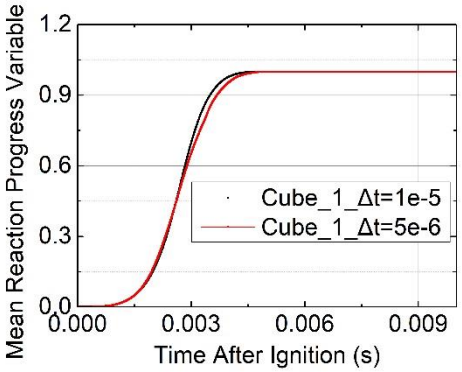

Figure 5-2 Results of time step sensitivity analysis using Mesh Cube_1

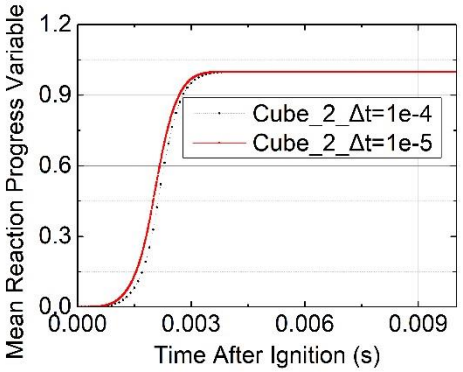

Figure 5-3 Results of time step sensitivity analysis using Mesh Cube_2

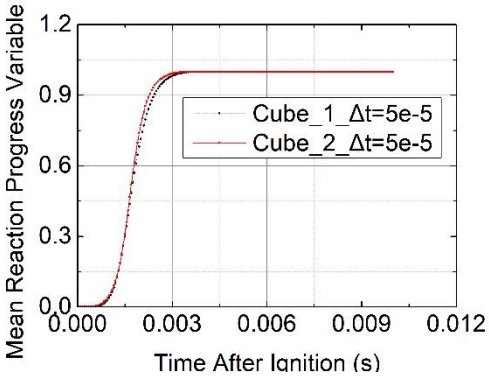

Figure 5-4 Results of mesh size sensitivity analysis using time step $\Delta t = 0.05\ ms$

Figure 5-5 shows the mean flame front evaluated at different instants using mesh Cube_1. The flame surface keeps very well as a sphere during the propagation process. This validates that the level set approach has been well implemented and the moving surface keeps smooth.

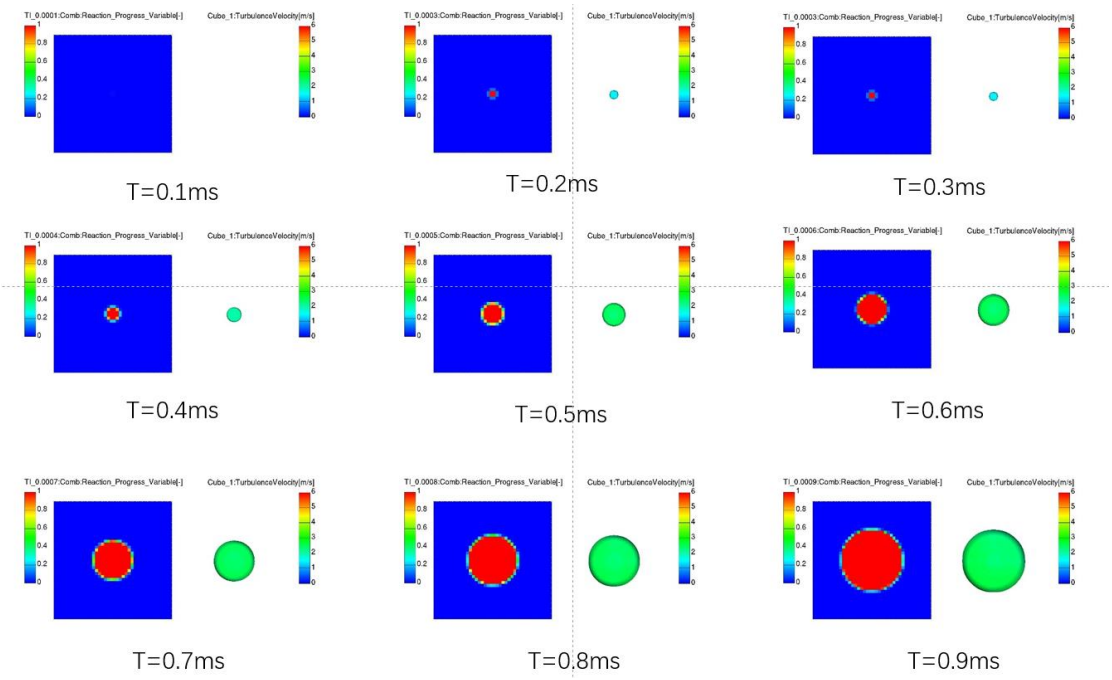

Figure 5-5 Mean flame front evaluated at different instants. The surface is colored with the turbulent burning velocity. Mesh: Cube_1

5.1.2 Hamamoto combustion bomb

In this numerical investigation, the mesh topology sensitivity of the model is discussed. A sphere with an initial radius of $r_0 = 3\,mm$ propagates through a flow field. Similar to section 5.1.1, the G-equation 4.4 becomes

$$\frac{\partial \tilde{G}}{\partial t} = s_T \left|\nabla \tilde{G}\right| \tag{5.3}$$

The computed domain is a closed cylinder of 125 mm diameter and 35 mm height. The flame front reconstruction in each element is performed differently. The G-field updating is performed not uniformly and the error increases with the number of re-initialization steps.

Table 5-2 Propagating sphere front in the Hamamoto combustion bomb - mesh and time step hierarchy

Mesh	Cell Number	Node number	Time step $\Delta t\ (ms)$
Hexa	50388	54100	0.1
Poly	64714	390494	0.1

Two different mesh topology strategies are adopted, i.e. the hexahedral mesh and the polyhedral mesh. They are shown in Figure 5-6. Exactly the same element volume is

difficult to achieve. Two meshes shown in Figure 5-6 are thereby the ones whose element volume are mostly similar to each other. The mesh and time step size information are summarized in Table 5-2. The spherical surface that is tracked throughout this simulation was initialized according to

$$G = -\sqrt{x^2 + y^2 + z^2} + r_0 \tag{5.4}$$

r_0 is the initial radius of the sphere, that was mentioned before. The iso-surface at different times of hexahedron mesh is depicted in Figure 5-7, where for polyhedron mesh is shown in Figure 5-8. Results are similar to the first test case, i.e. the shape of the spherical front of using the hexahedron mesh is well preserved. The one employing the polyhedron mesh has the same smooth and spherical moving flame surface. Through this way, the prediction ability of the model to different topology strategies is validated, which provides an obvious advantage for users in simulation.

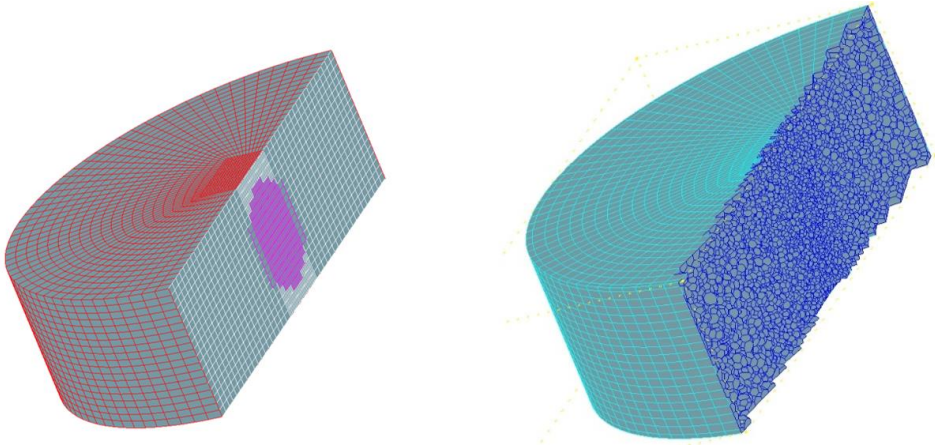

Figure 5-6 Meshes of the Hamamoto combustion bomb case

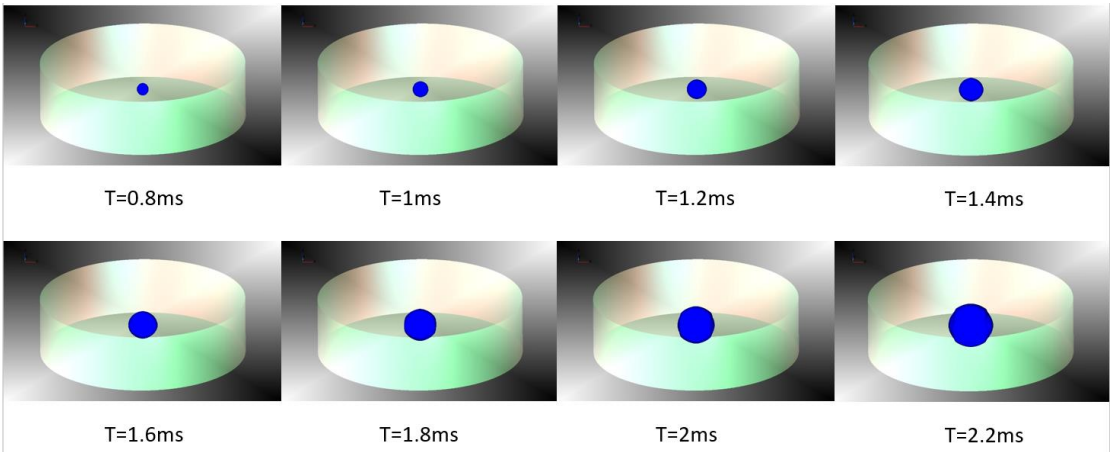

Figure 5-7 Simulated iso-surface (G_0) using the hexahedron mesh at different instants

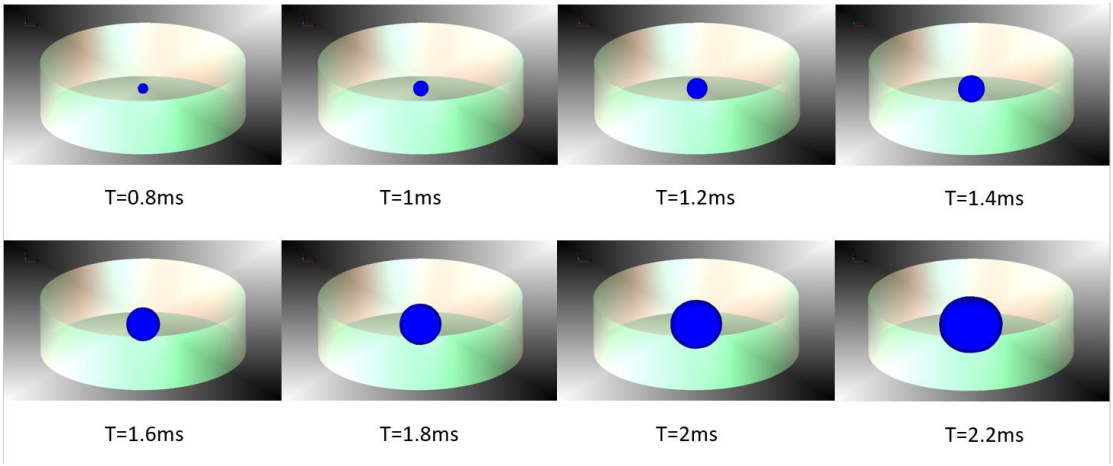

Figure 5-8 Simulated iso-surface (G_0) using the polyhedron mesh at different instants

5.2 Laminar combustion in the cylindrical combustion vessel

In this test case, the combustion process in a visualized combustion vessel used for measurement of the laminar burning velocity is modeled. An outwardly propagating spherical flame is generated in a constant-volume cylinder (CVM). An optimized Schlieren image processing method was established to record the combustion process in the vessel. The combustible mixture is ignited in the middle of the combustion vessel and propagates laminarly. The pressure in the combustion vessel increases as the heat releases during the combustion process, therefore, the temperature of the unburnt mixture T_u also increases. If the data acquisition window is quite narrow so that the pressure increase in cylinder is neglectable, the combustion process can be viewed as laminar.

5.2.1 Combustion vessel description

An 80-mm-diameter, 110-mm-length, stainless steel vessel was employed. The vessel could withstand 20 MPa steady pressure and 1000 °C temperature. An external heating system was designed for the premixed ignition test and the initial maximum temperature is 300°C. It had extensive optical access through two parallel windows on the bottom and top of the cylinder. The fuel used in this experiment is methane. The laminar burning velocity was derived from measurements of spherically expanding flame images captured using the high-speed Schlieren photography at, typically, 30000 frames per second (33 μs interval), time of exposure is 5 μs. Benchmark setup is shown in Figure 5-9. The influences of the ignition energy on the laminar burning velocity were investigated.

Under the condition of 0.3 MPa, 300K, $\phi = 1.0$, the measured unstretched laminar burning velocity of the methane flame is 0.24 m/s, which is consistent with the formulation proposed by Gu et al.[25] (see following)

$$s_L = 0.36\left(\frac{T_u}{T_0}\right)^{1.612}\left(\frac{p_u}{p_0}\right)^{-0.374} \tag{5.5}$$

where T_0 is the datum temperature and equals to 300K and p_0 the datum pressure equals to 0.1 MPa. As the initial pressure increases, the instability of the flame pattern

increases and the corresponding laminar burning velocity s_L decreases. The measured s_L at different initial pressures is summarized in Table 5-3.

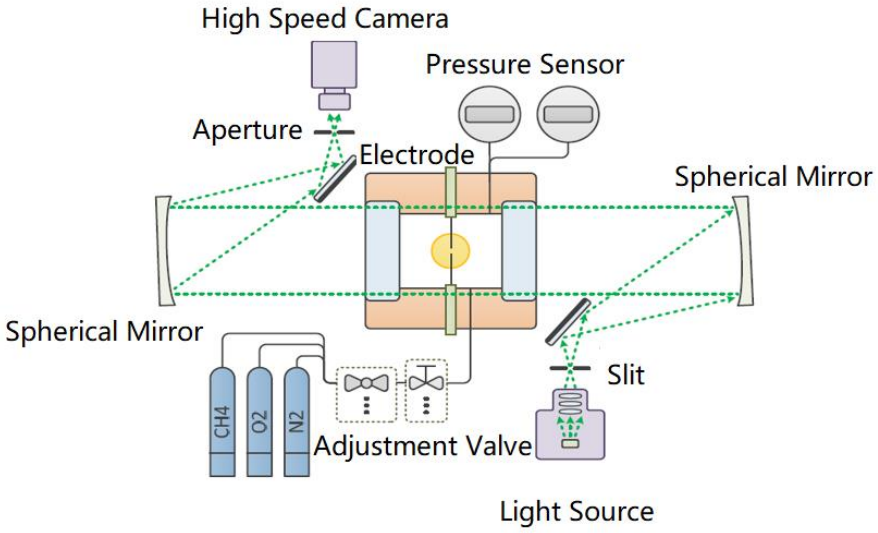

Figure 5-9 Benchmark for Combustion Vessel

Table 5-3 Measured unstretched laminar burning velocities of stoichiometric methane-air mixture at different initial pressures[82]

Initial pressure p_0 (MPa)	Unstretched laminar burning velocity s_L (m/s)
0.3	0.24
0.6	0.18
1.2	0.096

5.2.2 Simulation setup

As shown in Figure 5-10, hexahedron mesh was adopted for simulation and the information of the mesh hierarchy is summarized in Table 5-4. The averaged cell size is 1 mm and total elements are 640640. Three different initial pressures were simulated, i.e. 0.3 MPa, 0,6 MPa and 1.2 MPa.

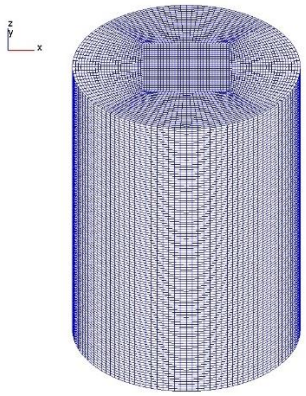

Figure 5-10 Hexahedron mesh of the laminar combustion vessel

Since the combustion process of interest is laminar, the turbulent kinetic energy and the turbulent dissipation rate are set to be infinitely small.

Table 5-4 Laminar combustion vessel - mesh statistics

Number of elements	Number of nodes	Averaged element size
640640	687834	1 mm

5.2.3 Results analysis

The flame front propagation obtained from the Schlieren images is shown in Figure 5-11. The equivalence ratio of the methane-air mixture is $\phi = 1$. The purity of the methane used in the experiment is 99.9%. The air used is the dried mixture of nitrogen and oxygen with the ratio 0.79:0.21. The ignition energy of different levels in Figure 5-11 was summarized in Table 5-5. For the sake of brevity, only the recorded flame radii at 0.3 MPa are shown. The detailed information for the other initial pressures can be found in the work of Lu H.'s dissertation[82]. From Figure 5-11 it can be seen, that the ignition energy has an obvious effect on the early phase of the flame propagation, i.e. the flame kernel generation. Higher ignition energy accelerated the formation of the flame kernel at the early stage after the ignition. However, the influence of the ignition energy on the laminar burning velocity is neglectable.

Based on this conclusion, the simulation focused only on the Normal ignition energy at three different initial pressures. The comparison of the measured and computed flame front at different time are depicted in Figure 5-12, Figure 5-13, and Figure 5-14.

Table 5-5 Averaged energy of different ignition levels

Ignition level	Averaged energy (mJ)
Normal	40
U-high1	213
U-high2	355
U-high3	422
U-high4	521
U-high5	580

The agreement between the simulated flame front and the experimental data is considerably good. The simulation could completely reproduce the flame front at the early stage of the combustion, where a slight over-estimation could be found during the end stage. This difference is probably caused by the constant laminar burning velocity used for the simulation. As the flame front propagates with the increase of the time, the temperature in the combustion vessel increases, according to equation 5.5, which leads to the bigger laminar burning velocity compared to the one as the model input. This difference also decreases with the increase of the initial pressure. Under the condition of $p_0 = 1.2\ \mathrm{MPa}$ shown in Figure 5-14, there is no obvious difference between the simulation results and the measured data.

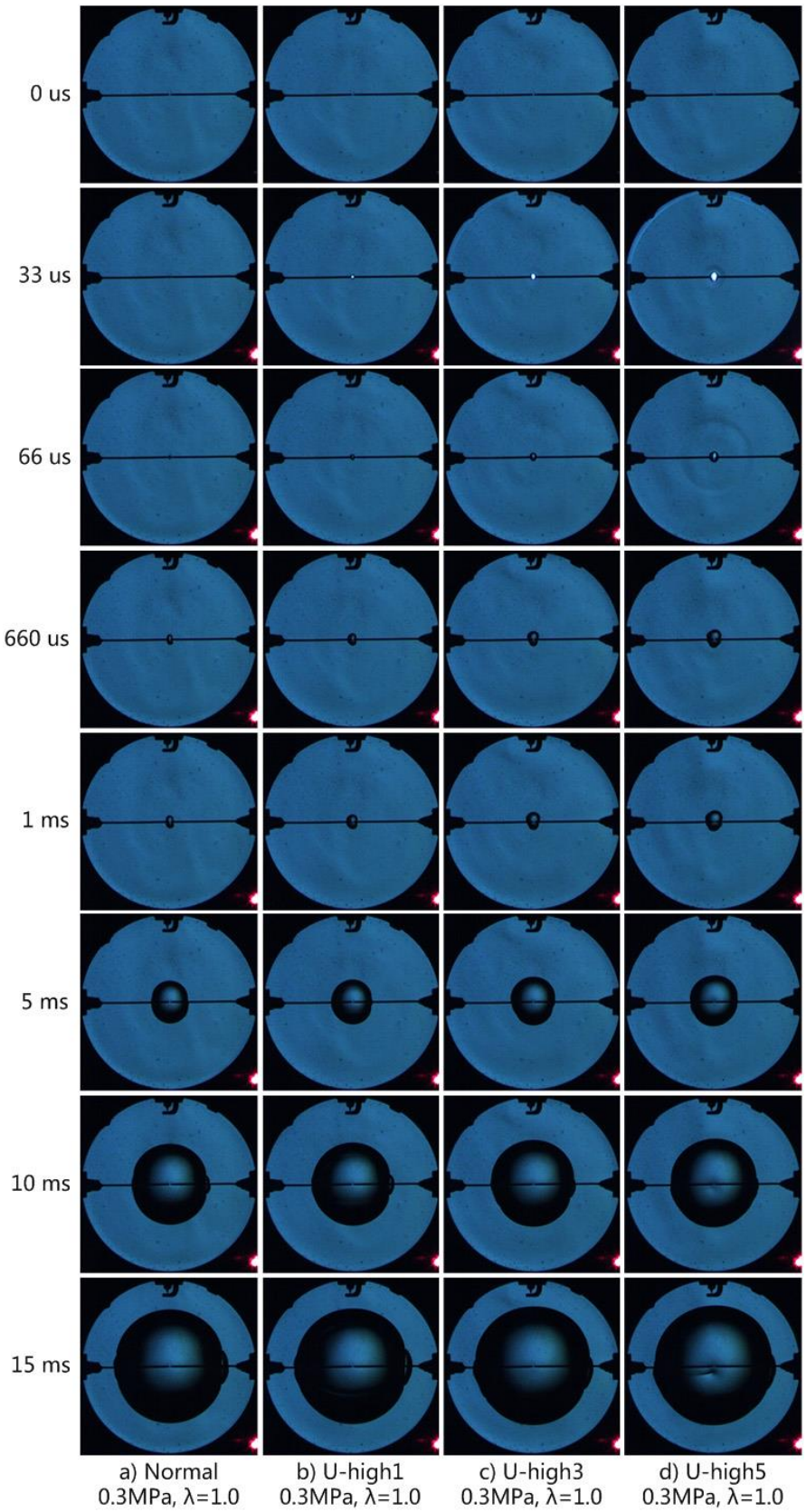

Figure 5-11 Schlieren images of the flame radii development using different ignition energies at $T_0 = 300\text{K}, p_0 = 0.3\ \text{MPa}, \phi$=1[82]

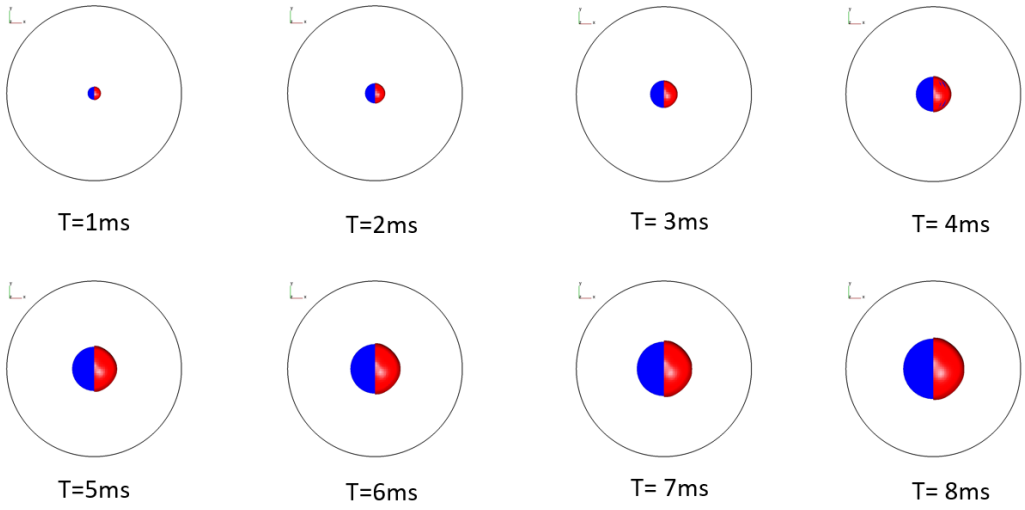

Figure 5-12 Comparison of the simulated flame front(red) with the experimental flame front(blue) at different instants after ignition for $s_L = 24\ \mathrm{cm/s},\ \phi = 1,\ p_0 = 0.3\ \mathrm{MPa}$

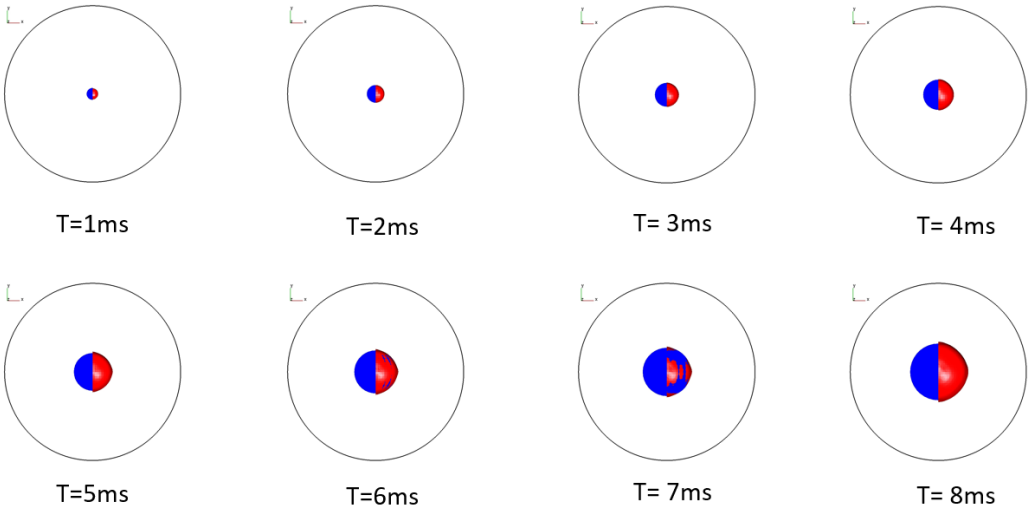

Figure 5-13 Comparison of the simulated flame front(red) with the experimental flame front(blue) at different instants after ignition for $s_L = 24\ \mathrm{cm/s},\ \phi = 1,\ p_0 = 0.6\ \mathrm{MPa}$

Thus, the model is also suitable for the simulation of laminar combustion phenomenon. The robustness and the accuracy of the model is considerably good.

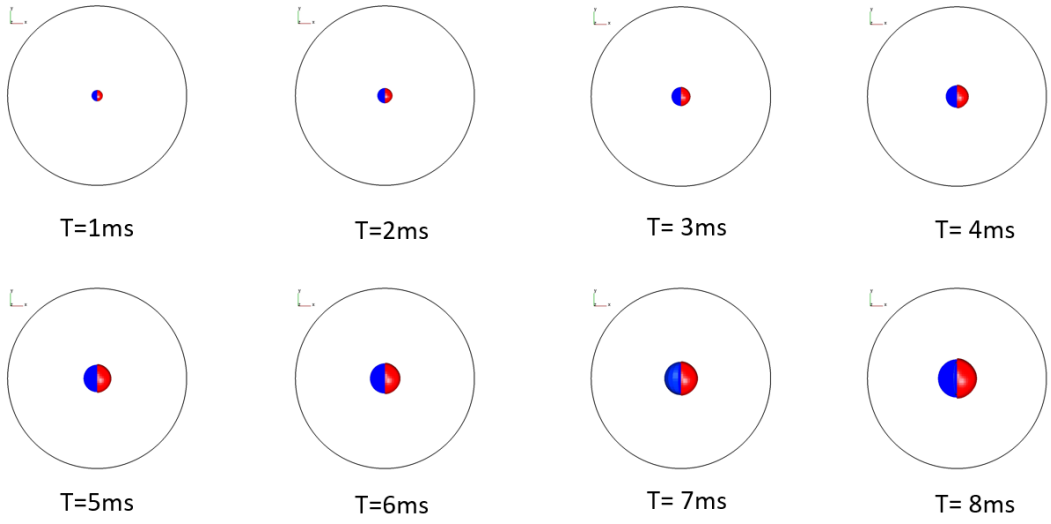

Figure 5-14 Comparison of the simulated flame front(red) with the experimental flame front(blue) at different instants after ignition for $s_L = 24\ \mathrm{cm/s},\ \phi = 1,\ p_0 = 1.2\ \mathrm{MPa}$

5.3 Pancake engine

5.3.1 Engine Descriptions

This engine was initially presented by Alkidas[83] to investigate the heat transfer characteristics of the spark ignition engine. It has been derived from a four-stroke V8 spark-ignition engine featuring a disc-shaped combustion chamber[84][85][86]. The spark plug is located at the center of the cylinder head. The following geometry specifications are given in references[84][85][86], shown in Table 5-6. This test case is especially interesting for the validation of the combustion process and wall heat tranfer models designed for practical internal combustion engine applications, since the very complex combustion process occurs in a relatively simple geometry in SI engines.

Table 5-6 Geometrical Data of the Pancake Engine

Bore	105.0 mm
Stroke	95.25 mm
Connecting rod length	158.0 mm
Cylinder displacement	0.82 L
Compression ratio	8.56
TDC clearance	12.6 mm
Spark Plug Location	Central on cylinder head

The following operating point has been chosen for the benchmark, as given in Table 5-7.

Table 5-7 Operating Condition

Engine Speed	1500 r/min

Fuel	Propane, C_3H_8
Equivalence Ratio	0.87
Spark Timing	27° CA BTDC
Intake valve closing	117° CA BTDC
Volumetric efficiency	40 %

The volumetric efficiency has been calculated using the ratio between the actual mass of air supplied to the cylinder per cycle and the theoretical mass of the air when the displacement volume is filled by air at atmospheric conditions, i.e. 288 K and 101 kPa. Investigations regarding the numerical simulation of this test case were performed by Tan et al. [84], Han et al.[85], Toninel et al.[87] and Linse[32].

5.3.2 Han-Reitz heat transfer wall model

The heat transfer wall model used in this thesis is based on Han and Reitz's work[85]. A temperature wall function that includes the thermodynamic variations of the gas density and the increase of the turbulent Prandtl number in the combustion boundary layer was derived. Assumptions adopted to derive the model are:

1) Gradients parallel to the wall are significantly small and can be neglectable compared to those normal to the wall;
2) Pressure ingredients are neglected;
3) The fluid velocity is in the tangential direction of the wall surface;
4) Radiation heat transfer is neglected;
5) Ideal gas assumption;
6) Viscous dissipation and the Dufour effects (thermal diffusion)[88] are neglected.

The energy conservation equation can be written as

$$\frac{\partial q}{\partial y} = -\rho c_p \frac{\partial T}{\partial t} + \frac{dp}{dt} - Q_c \tag{5.6}$$

where

$$q = -(k + k_t)\frac{\partial T}{\partial y} \tag{5.7}$$

Using the normalized quantities

$$\nu^+ = \frac{\nu_t}{\nu}; y^+ = \frac{u^* y}{\nu}; Q_c^+ = \frac{Q_c \nu}{q_w u^*} \tag{5.8}$$

And integrating the equation 5.6 from the wall, neglecting the source term, the equation for the wall heat flux is written as

$$q_w = \frac{\rho c_p u^* T \ln\left(\frac{T}{T_w}\right)}{2.1\ln(y^+) + 2.5} \tag{5.9}$$

For the sake of brevity, only the essence of the formulations for the heat transfer wall model is discussed here. The model details can be found in the reference[85].

By comparing to the model that excludes the gas compressibility, it can be seen that the models excluding the gas compressibility significantly under-predict the heat transfer when the engine is fired, while the model developed by Han and Reitz that includes the gas compressibility reproduces the measurement well. The effect of

chemical heat release is included in the present model. However, the comparison shows that the neglect of the heat release source in the energy equation would not cause large errors in wall heat flux predictions for the engine case considered.

5.3.3 Simulation setup

A hexahedron mesh was applied. The geometrical structures of the mesh are shown in Figure 5-15. The typical mesh size is 1 mm and the numerical time step used is 0.1 crankshaft angle degree (CAD), i.e. about 11 us since the engine speed is 1500 r/min.

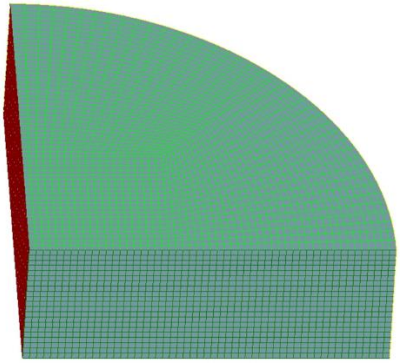

Figure 5-15 Hexahedron Mesh Geometry of Pancake Engine at 30°CA BTDC

The initial conditions were defined based on Toninel et al.[87]. The turbulent kinetic energy was calculated by the following equation

$$k = 1.5 \cdot (0.4 \cdot \overline{s_P})^2 \tag{5.18}$$

where $\overline{s_P}$ is the mean piston speed.

The simulation solver settings are summarized in Table 5-8. Two velocity models, i.e. Ewald velocity model and GFWI velocity model, were used to make a cross-comparison.

Table 5-8 Initial conditions of calculation

Spark ignition model	27° BTDC
Combustion model	Eulerian Flame Tracking Model
Turbulence model	k-zeta-f
Heat transfer wall model	Han-Reitz model
Turbulent kinetic energy	5.44 m^2/s^2
Turbulent dissipation rate	2084.88 m^2/s^3
density	2.32888 kg/m^3
Initialization mode	Uniform initialization
Initial pressure	5.305 bar
Initial temperature	805 K

5.3.4 Results analysis

The comparison between the computed in-cylinder pressure of two different velocity models and the measured pressure histories is plotted in Figure 5-16. An encouraging agreement with the measured data was found. Compared to the Ewald model, the

GFWI velocity model has better performances. The GFWI model predicted the early stage of the combustion more accurately and almost the same maximum in-cylinder pressure like the measured data. However, both models had a slight overestimation of the pressure increase during the main stage of the combustion.

The heat release rate showed this trend more clearly, which is depicted in Figure 5-17. Since the measured pressure histories has only ten pair data, the curve of the measure heat release rate is not smooth. The early stage of the combustion was overestimated by both models with the higher heat release rate compared to the measured data. However, the GFWI model predicted the better agreement of the heat release rate with the measured data at the main combustion stage and the combustion phenomena during the expansion stroke.

Additional details about the flame structure and the flame development are summarized in Figure 5-18 and Figure 5-19, which show the predicted flame front location in the combustion chamber at every 2° CAD after the spark (spark occurs at 27° BTDC). The flame front surface was colored by the turbulent burning velocity. The mean flame front surface predicted by both velocity models is smooth. However, it is obviously to be noticed that the GFWI model predicts a slower s_T when the flame front reaches the wall (the green-colored area of the whole flame surface), which is more reasonable.

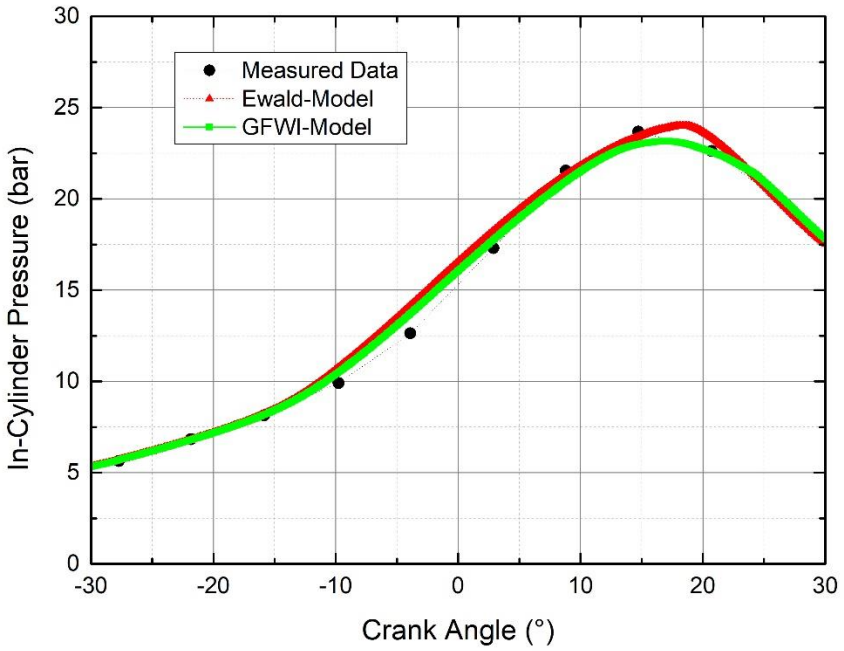

Figure 5-16 Comparison of simulated In-cylinder Pressure histories with experimental data

for the pancake engine

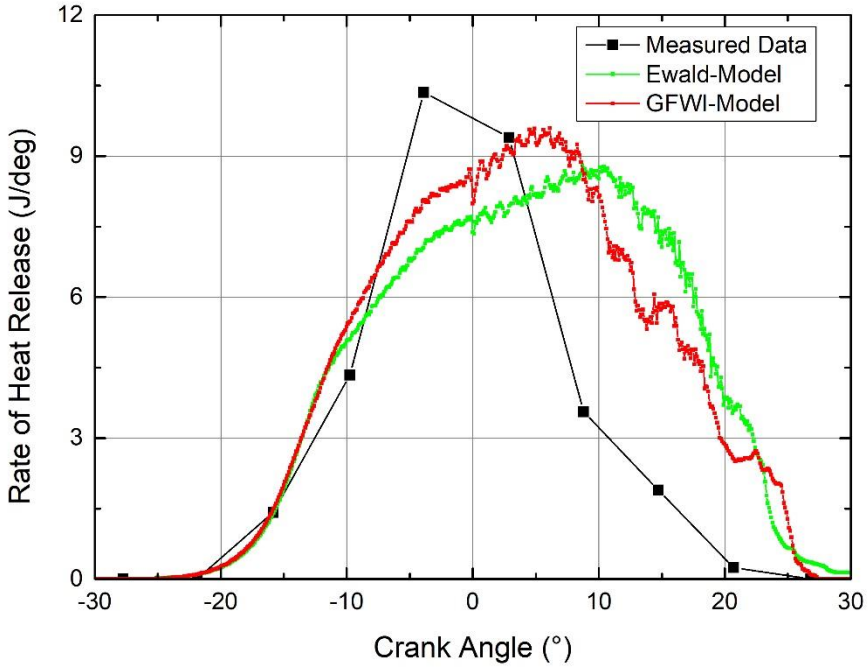

Figure 5-17 Comparison of simulated heat release rate histories with experimental data for the pancake engine

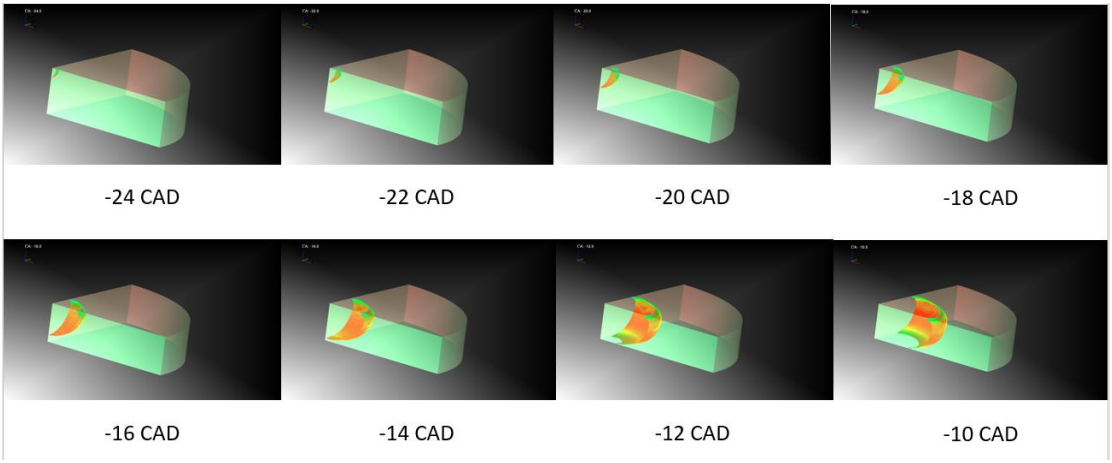

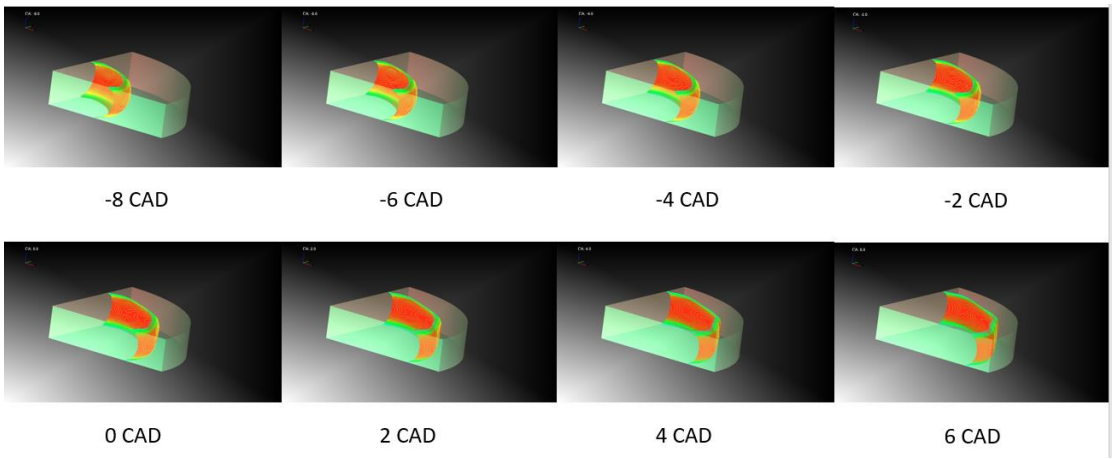

Figure 5-18 Flame Front Propagation at different crank angle for the pancake engine using Ewald velocity model

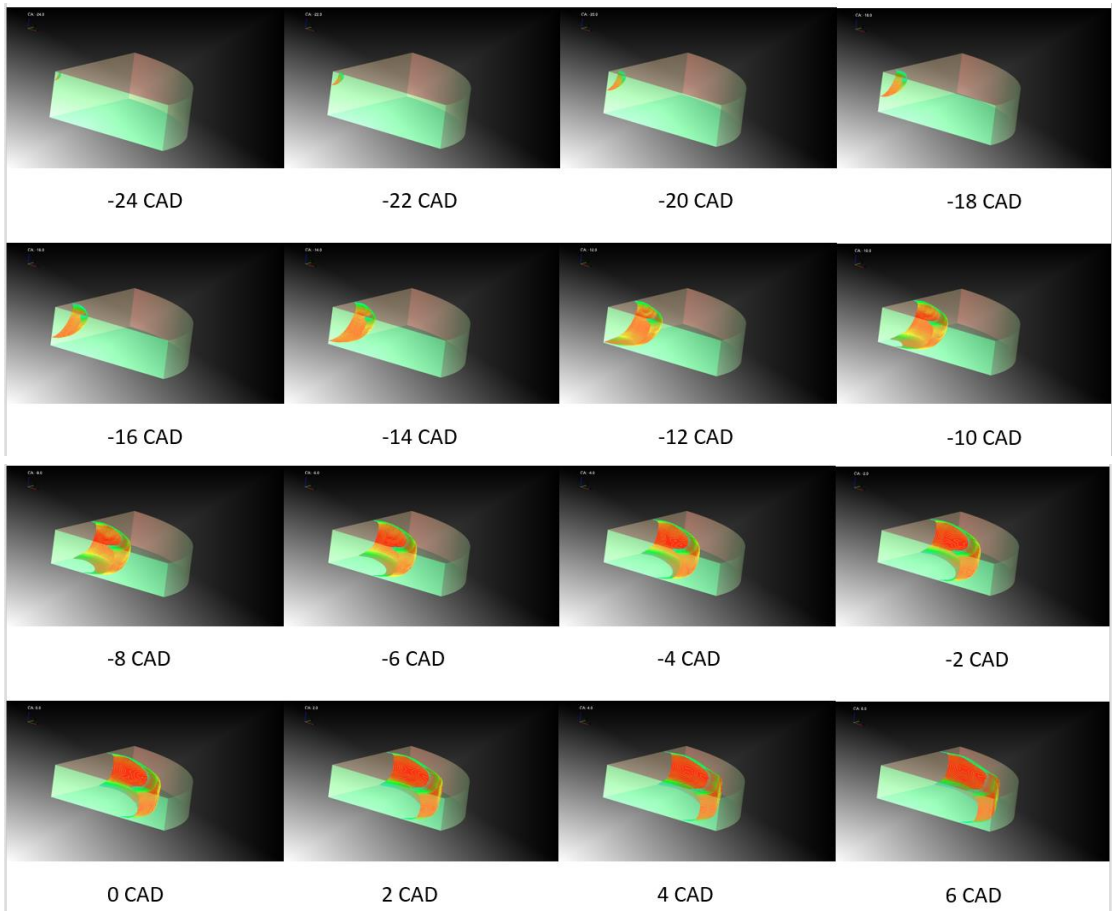

Figure 5-19 Flame Front Propagation at different crank angle for the pancake engine using GFWI velocity model

The definition of y^+ is given by Han and Reitz[85] and reads as

$$y^+ = \frac{u^* y}{\nu} \tag{5.19}$$

Therein, u^* is derived from the turbulent kinetic energy k. y is the distance of the flame front to the wall. ν is the kinematic viscosity of the investigated mixture. y^+

decreases when the flame front propagates, because the gas viscosity increases as the gas temperature increases by heat releasing. As shown in Figure 5-20, two models have the same y^+ at about 10 CAD BTDC. After this, the GFWI velocity model predicts a higher y^+ value until 12 CAD ATDC.

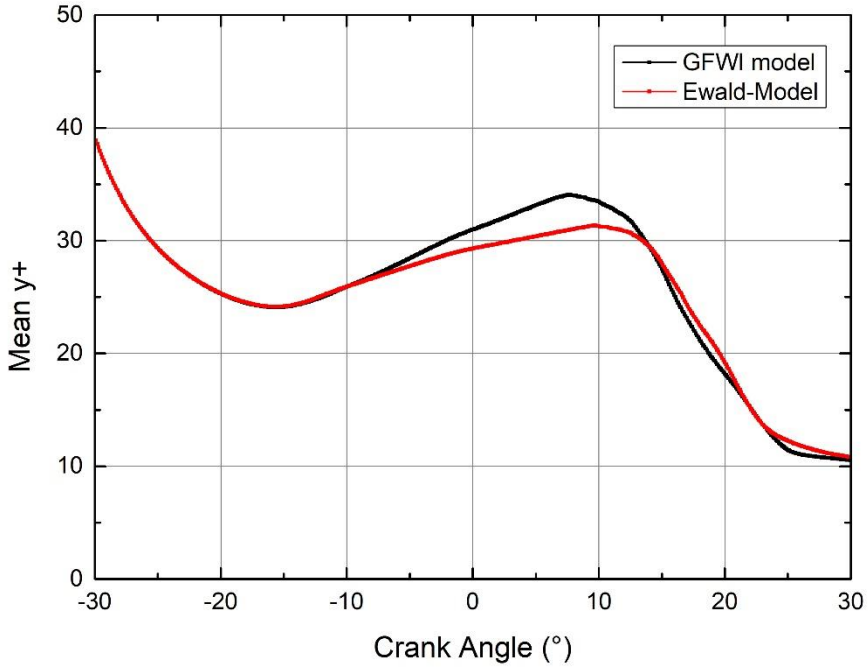

Figure 5-20 Comparison of y^+ using two different turbulent burning velocity models

Based on results from this case, it is clear that the GFWI velocity model can reproduce the combustion process occuring in the ICEs better. For the following validation process, only the GFWI velocity model will be adopted.

5.4 Gasoline direct injection spark ignition engine

Nowadays, CFD-tools provide a strong support for the development of the high-performance engines. Numerical studies can obviously reduce the time and the cost of the development process. If the accuracy of the model is validated for the existing practical engines, the prediction based on the same model for the future development activities is meaningful. In this section, the test case is an AVL DISI engine. Experiments were carried out on the test bench carefully and reliable for the comparison with simulation results.

5.4.1 Engine description

The investigated engine is an AVL Prototype single-cylinder gasoline engine with direct injection and homogeneous charge combustion, shown in Figure 5-21. The engine allows for variable valve timing. Engine specifications are presented in Table 5-9. For the analysis of the gas exchange process it is important to combine low- and high-pressure indication. The simultaneous use of a piezoelectric pressure sensor in the

combustion chamber and piezoresistive absolute-pressure sensors in the intake/exhaust system was necessary to calculate the mass flow rate at the inlet and outlet as well as the trapped residual gas mass in the cylinder by means of an 1D gas exchange simulation.

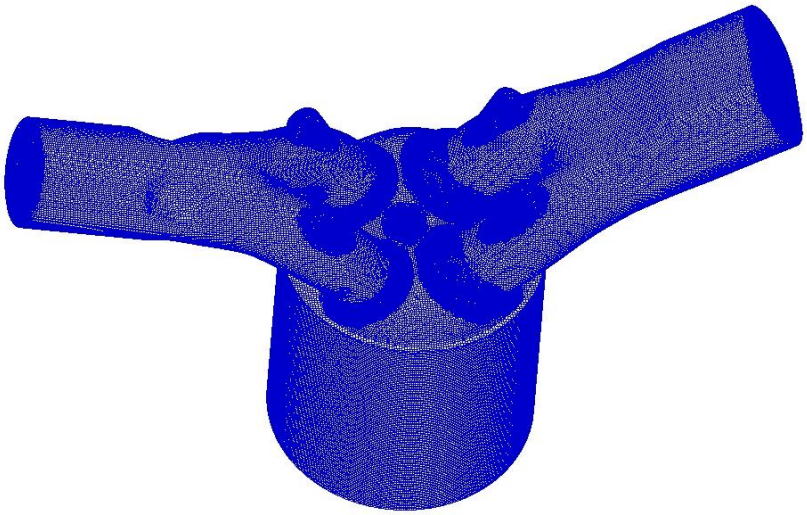

Figure 5-21 Geometrical structure of the AVL single-cylinder prototype engine

Table 5-9 Engine specifications

Engine type	Gasoline engine, 4-stroke
Bore	86 mm
Stroke	86 mm
Compression Ratio	12.5
Valve number	4 valves (2 intake 2 exhaust valve)
Cylinder number	Single cylinder

5.4.2 1D heat release analysis

The heat release analysis is based on the measured cylinder pressure in the internal combustion engine. AVL BOOST calculates the characteristic heat release rate $dQ_{chem}/d\alpha$ from the measured cylinder pressure history under the assumption of a single-zone cylinder model. Based on a thermodynamic single-zone model it is assumed that the combustion chamber is ideally mixed. Because of the homogenous gas mixture, no spatial information like mixture formation or temperature distribution is available and the thermodynamic state of the fluid is only a function of time. The advantage of this simple thermodynamic model is its low computational cost. The governing equation for the mass of the single-zone model solved by AVL BOOST is given by

$$\frac{dm_{cyl}}{d\alpha} = \frac{dm_{in}}{d\alpha} + \frac{dm_{exh}}{d\alpha} + \frac{dm_f}{d\alpha} + \frac{dm_b}{d\alpha} \tag{5.20}$$

Where the changes of the trapped cylinder mass m_{cyl} is related to the mass from the intake valves m_{in} and exhaust valves m_{exh}, the injected fuel mass m_f, and the blow-by mass m_b due to the leakage.

The energy equation reads

$$\frac{dU_{cyl}}{d\alpha} = \frac{dU_w}{d\alpha} + \frac{dQ_{chem}}{d\alpha} - \frac{pdV}{d\alpha} + \frac{dm_{in}}{d\alpha}h_{in} + \frac{dm_{exh}}{d\alpha}h_{exh} + \frac{dm_f}{d\alpha}h_f + \frac{dm_b}{d\alpha}h_b \quad (5.21)$$

where U_{cyl} is the internal energy of the trapped mass in the cylinder, $\frac{dU_w}{d\alpha}$ the wall heat flux, $\frac{dQ_{chem}}{d\alpha}$ the heat release rate of the combustion process, $\frac{pdV}{d\alpha}$ the displacement work, $\frac{dm_{in}}{d\alpha}h_{in}$, $\frac{dm_{exh}}{d\alpha}h_{exh}$, $\frac{dm_f}{d\alpha}h_f$, $\frac{dm_b}{d\alpha}h_b$ the enthalpy of the mass from the intake valves, exhaust valves, injected fuel and the blow-by mass.

The heat release rate $dQ_{chem}/d\alpha$ is modeled by an empirical correlation called Vibe function and yields

$$\frac{Q_{chem}}{Q_{chem,total}} = 1 - \exp\left[-a\left(\frac{\alpha - \alpha_{SOC}}{\Delta\alpha_c}\right)^{m+1}\right] \quad (5.22)$$

where $Q_{chem,total}$ is the total chemical energy containing in the mixture. However, due to the incomplete combustion, not all of the energy can be released. Therefore, a is a quantity accounting for the incomplete combustion. α_{SOC} is the start of the combustion and $\Delta\alpha_c$ the duration of the combustion process. m is the shape parameter. Differentiating the equation 5.22 leads to the instantaneous heat release rate

$$\frac{dQ_{chem}}{d\alpha} = a \cdot Q_{chem,total} \cdot (m+1) \cdot \left(\frac{\alpha - \alpha_{SOC}}{\Delta\alpha_c}\right)^m \cdot \exp\left[-a\left(\frac{\alpha - \alpha_{SOC}}{\Delta\alpha_c}\right)^{m+1}\right] \quad (5.23)$$

Based on the equation 5.23, using the measured in-cylinder pressure histories as model input, according to the model built in the AVL BOOST, as shown in Figure 5-22,

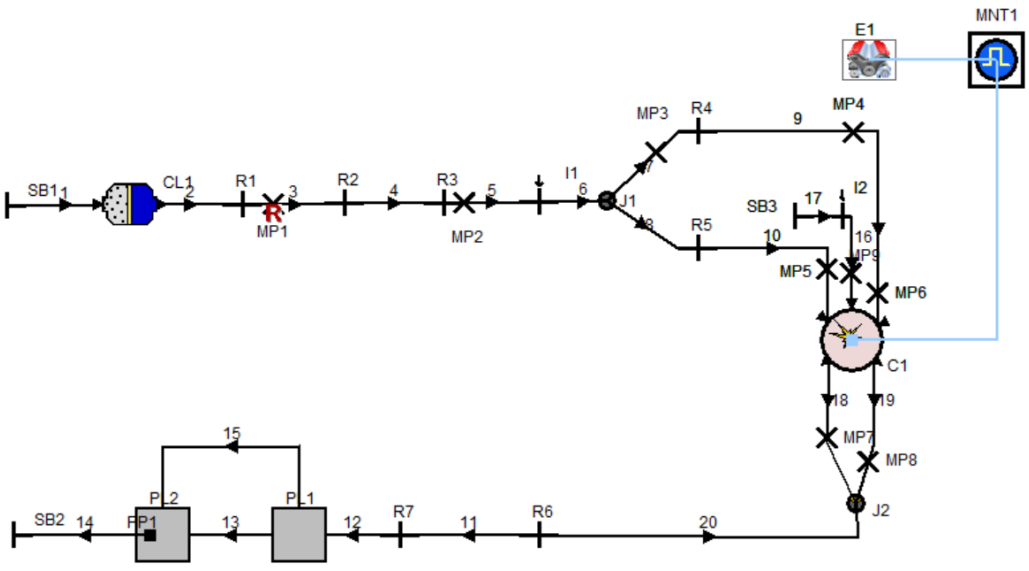

Figure 5-22 1D-Heat Release Analysis, AVL BOOST model

the chemical heat release rate during the combustion process can be derived. Pipe 9 and Pipe 10 represent the intake manifolds, Pipe 18 and Pipe 19 the exhaust manifolds. I2 is the injector, the length of the Pipe 16 is set to be 0 mm such that the direct injection

is modeled. The central part of the model is the cylinder C1. This unit includes the geometrical information of the combustion chamber and the characteristics of the combustion process, such as start of combustion (SOC), combustion duration (CD), heat transfer etc.

The results of the 1D simulation were used to define the boundary and initial conditions of the inflows and outflows at the intake and exhaust ports for every engine operating point.

5.4.3 Numerical setup

The meshes used for the simulation are a hexahedron mesh and a polyhedron mesh, that are depicted in Figure 5-23. Different load points were investigated to evaluate the model. Detailed information is given in Table 5-10. Four different engine speeds, i.e. 1250 r/min, 1500 r/min, 2000 r/min and 3000 r/min were chosen.

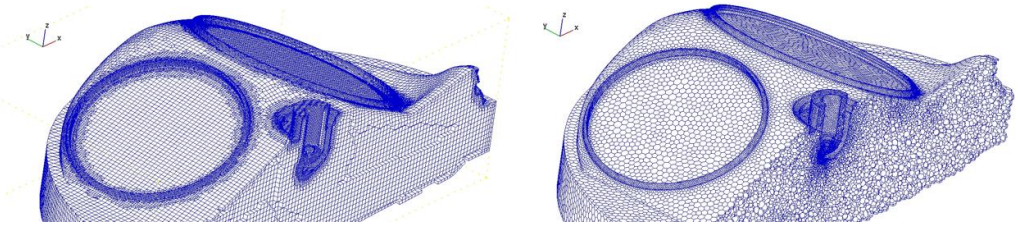

Figure 5-23 Hexahedron mesh(left) and polyhedron mesh(right) for AVL prototype engine at firing TDC

Table 5-10 Engine operating points for the combustion validation

Operating point	Engine speed (r/min)	Ignition timing	Equivalence ratio
1	1250	695 CA	1
2	1500	703 CA	0.93
3	2000	697.4 CA	1
4	3000	696.4 CA	0.98

For the operating point 4, two different meshes were adopted to investigate the topology sensitivity of the Eulerian Flame Tracking Model. Figure 5-24 gave the

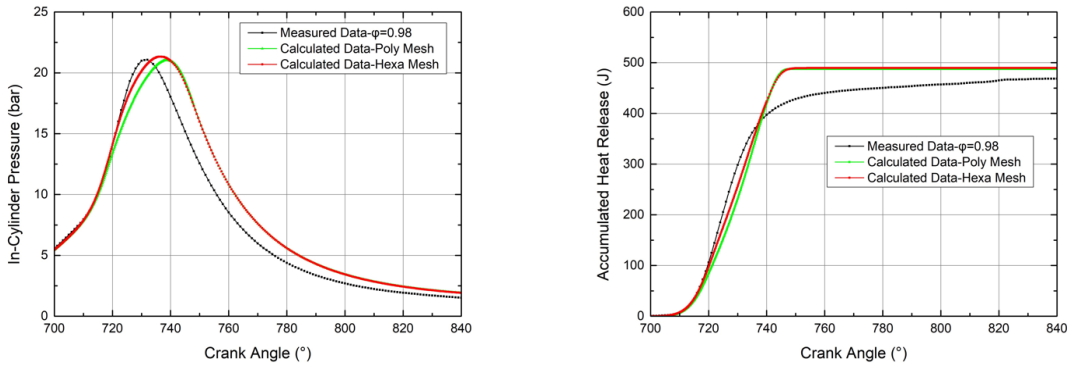

Figure 5-24 Comparison of simulated and measured in-cylinder pressure traces(left) and the

accumulated heat release(right) of the engine load point 4: n=3000 r/min, $\phi = 0.98$, ignition timing=696.4 CAD

comparison of the in-cylinder pressure histories and the accumulated heat release. Two different meshes can reproduce the combustion process in the combustion chamber very well. The difference between two meshes are neglectable. Based on this, for the other operating points, only the polyhedron mesh is used, since it is possible to refine the mesh around the spark plug with a fine transition to the coarse size further way.

The turbulence model used in this test case is the most widely used $k-\varepsilon$ model. It has been proven to be stable and numerically robust over years of application on the practical engine simulations.

5.4.4 Gas exchange simulation

In order to investigate the turbulent combustion phenomenon in DISI engines, it is necessary to verify that processes such as gas exchange, mixture formation, and charge motion are well captured by the physical models in the CFD simulation. In the following, computational results of the 3D-CFD gas exchange simulation are presented and analyzed. One engine operating point is investigated. An overview of the corresponding operating conditions is given in Table 5-11.

Table 5-11 The investigated engine operating point information

Engine speed	2000 r/min
Equivalence ratio ϕ	1
EVO	117.36 CA
EVC	361.81 CA
IVO	373.64 CA
IVC	607.10 CA
Start of Calculation	133 CA
IMEP	2.86 bar

The computation was started at 133 CA. In the computational domain, the initial velocity was set to zero. The temperature and pressure in both the combustion chamber and the exhaust port were initialized according to the results of the 1D results. In the entire computational domain, the residual exhaust gas was initialized according to the engine out equivalence ratio of the corresponding operating point. The fuel was injected during the intake stroke and the mixture in the combustion chamber can then be viewed as homogenous.

Figure 5-25 shows the cylinder pressure histories of the gas exchange process. The simulated in-cylinder pressure is compared with the measured data for the investigated load point. The data is evaluated in the range from 133 CAD to 500 CAD. The pressure rise due to the combustion is addressed in the subsequent section. It can be seen, that the computed pressure histories are in reasonable agreement with the experimental data. Minor differences are observed during the exhaust valves close and intake valves

open period. This is due to the simplified wall heat transfer model of the 1D gas exchange model, which leads to inconsistencies in the boundary conditions. The 1D model computes slightly higher wall fluxes than the 3D model. This is especially true during the exhaust valves close phase. However, the simulated in-cylinder pressure is consistent with the measured data after intake valves open. This is encouraging for the same in-cylinder conditions before ignition.

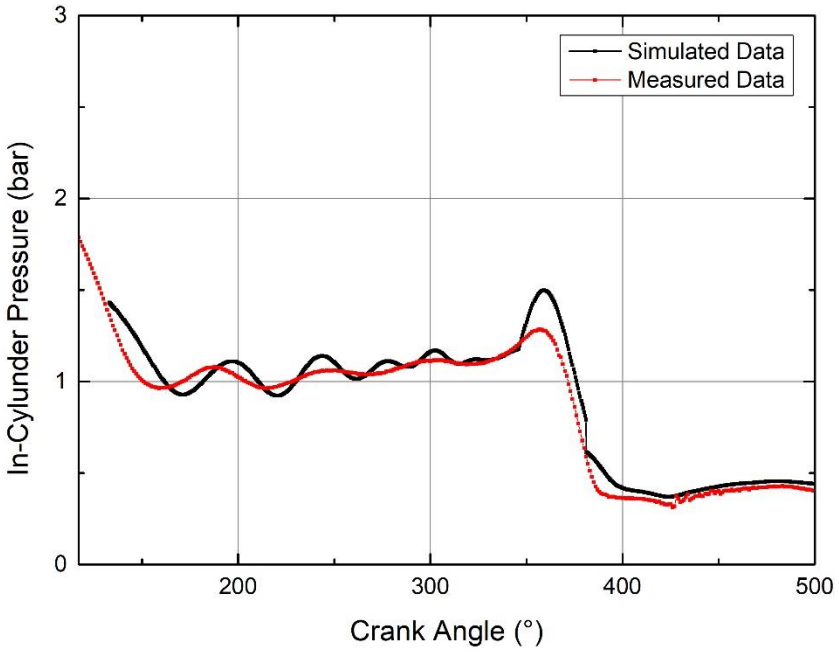

Figure 5-25 Cylinder pressure histories of the gas exchange simulation of the investigated operating point

5.4.5 Investigation of the turbulent flame propagation and flame structures

The level-set based EFTM model presented in chapter 4 was applied to simulate the combustion process in a single-cylinder DISI engine. The simulation results of the implemented model in AVL FIRE™ for the turbulent premixed combustion were validated against experimental data, special emphasis was put on the characterization of the interaction between the turbulence and flame propagation.

Figure 5-26 compares the computed in-cylinder pressure histories of the engine operating point 1 with the measured data. The pressure rise due to the combustion process is well reproduced, especially during the early and main stage of the combustion process. The simulated peak pressure is in very good agreement with the experimental record but the corresponding crank angle is slightly postponed. This offset persists during the early stage of the expansion stroke. This deviation is most probably due to an overestimated flame quenching model that accounts for the interaction between the flame and the wall. The further improvement of this Flame-Wall interaction model is however out of the scope of this thesis which is left for the

future work.

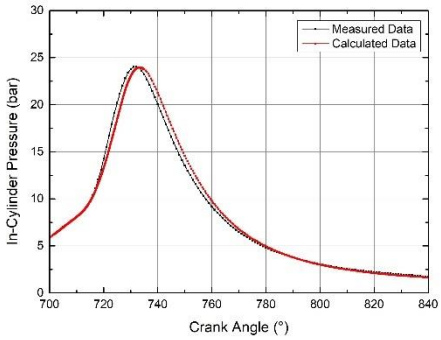

Figure 5-26 Comparison of simulated and measured cylinder pressure traces of the engine operating point 1: n=1250 r/min, ϕ=1

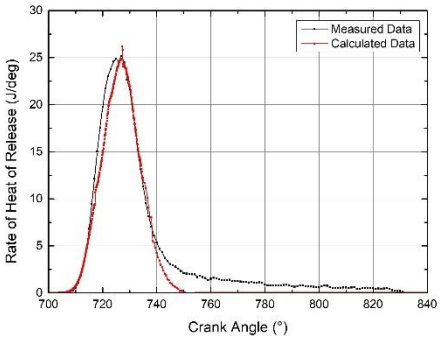

Figure 5-27 Comparison of simulated and measured heat release rate of the engine operating point 1: n=1250 r/min, ϕ=1

The energy containing in the combustible mixture is released with the propagation of the flame front. Figure 5-27 shows the calculated heat release rate and is compared with the experimental data. The measured heat release rate is obtained by employing the 1D heat release analysis based on AVL BOOST (see section 5.4.2). As expected, the overall shape of the calculated heat release rate is in very good agreement with the measured data.

The accumulated heat release is derived from the integration of the heat release rate through the whole combustion duration. The equation yields

$$Q_{chem} = \int_{\alpha_{SOC}}^{\alpha_{SOC}+\Delta\alpha_C} \dot{Q}_{chem} d\alpha \tag{5.24}$$

Figure 5-28 plots the simulated heat release of the engine operating point 1. The slope of the curve corresponds to the combustion process and looks reasonable, which indicates the combustion process in the combustion chamber is well reproduced. The point in the Figure 5-28 is the theoretical maximum available energy containing in the fuel. The calculated fuel mass is m_c=9.83 mg and the lower heating value of the gasoline is 43.4 MJ/kg. The energy released through the combustion process can be calculated using the equation

$$Q_{th} = m_c \cdot LHV = 9.83 \cdot 43.3 = 426.622\,J \tag{5.25}$$

It can be seen that the calculated released energy is in good agreement with the theoretical data, which indicates that the mixture burned completely and almost all available energy was released.

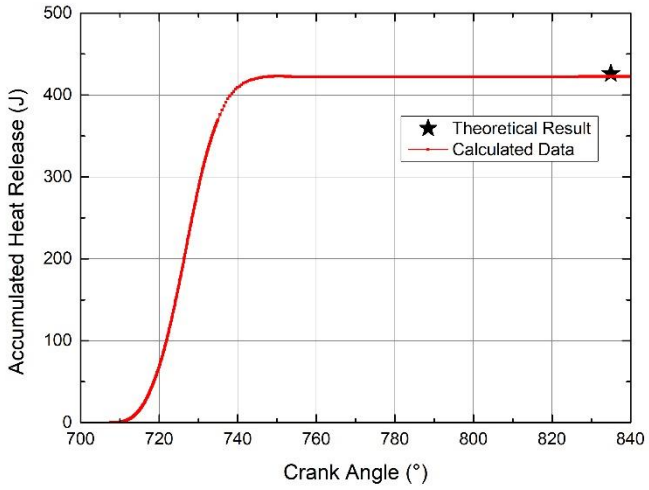

Figure 5-28 Comparison of simulated accumulated heat release and the theoretical released energy of the engine operating point 1: n=1250 r/min, ϕ=1

The mean flame front for the engine operating point 1 at different instants is shown in Figure 5-29. The flame front is colored with the turbulence velocity. It can be observed that after the spark ignition, the flame propagates faster towards the direction of the injector, which is indicated by the higher turbulence velocity. This results from the higher turbulence level in this area because of the specifically designed piston, which leads to higher turbulence level.

For the operating 2 (Figure 5-30, Figure 5-31), 3 (Figure 5-32, Figure 5-33) and 4 (Figure 5-34, Figure 5-35), the overall good agreement of the simulated in-cylinder pressure histories, rate of heat release to the experimental data is achieved. However, an obvious deviation of the calculated heat release rate from the measured data was observed in load point 2 and 4. A detailed comparison is plotted in Figure 5-36 by rescaling the x-axis. The rezone procedures took place at 707 CAD, 717 CAD, 727 CAD etc. It can be seen that the slope of heat release rate changed obviously after the rezone at 717 CAD. An obvious jitter of heat release rate can also be observed at 727 CAD and 737 CAD. Based on this conclusion, the numerical techniques should be adopted in the future to deal with this problem, in order to achieve the consistent flow field and combustion after rezone.

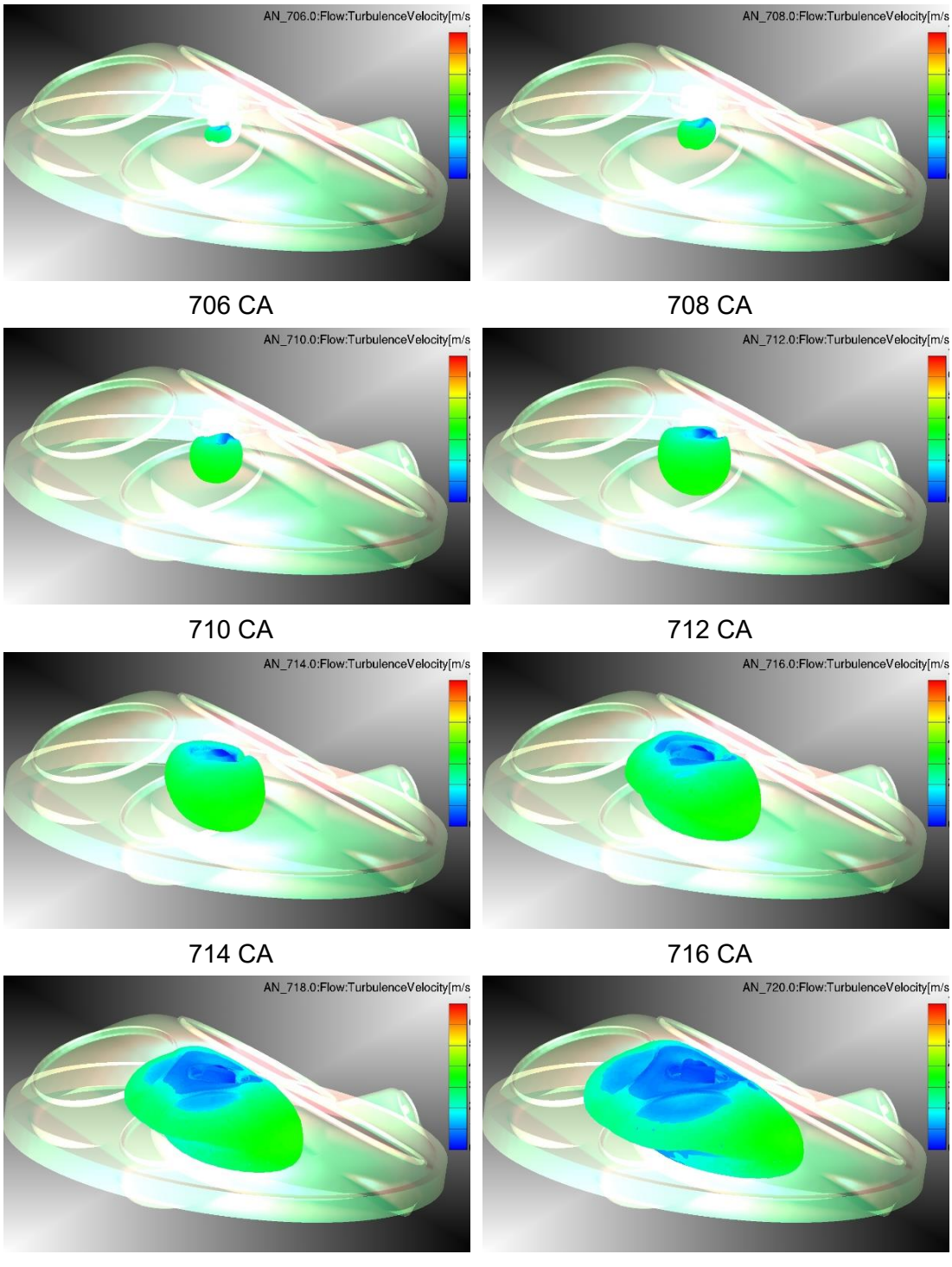

Figure 5-29 Mean flame front at different crank angle. The surface is colored with the turbulence velocity. Engine operating point 1: n=1250 r/min, ϕ=1

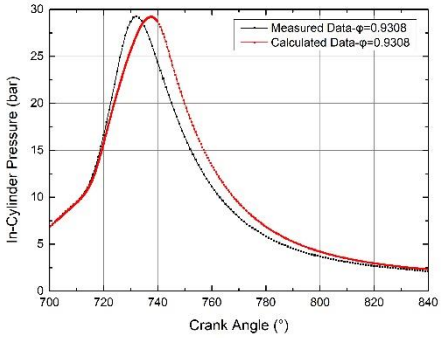

Figure 5-30 Comparison of simulated and measured cylinder pressure of the engine operating point 2: n=1500 r/min, ϕ=0.93

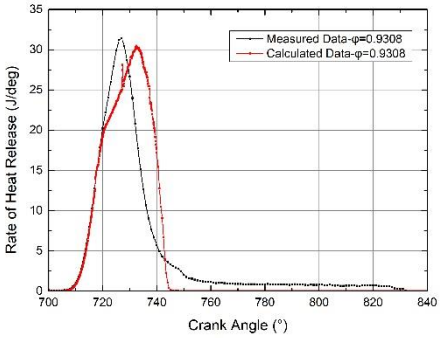

Figure 5-31 Comparison of simulated and measured heat release rate of the engine operating point 2: n=1500 r/min, ϕ=0.93

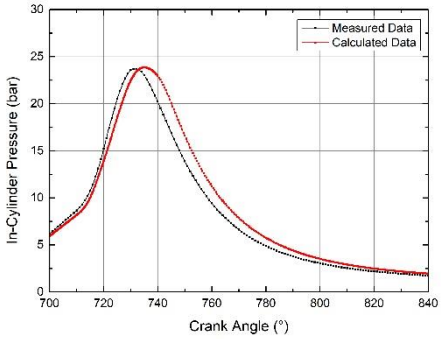

Figure 5-32 Comparison of simulated and measured cylinder pressure of the engine operating point 3: n=2000 r/min, ϕ=1

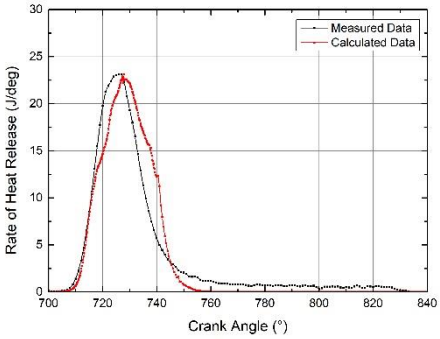

Figure 5-33 Comparison of simulated and measured heat release rate of the engine operating point 3: n=2000 r/min, ϕ=1

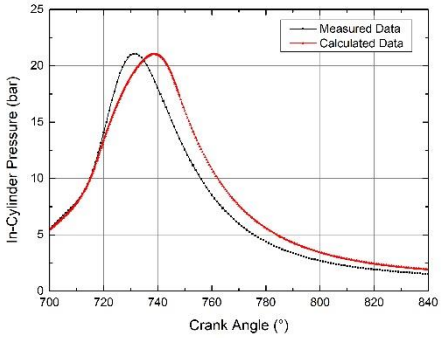

Figure 5-34 Comparison of simulated and measured cylinder pressure of the engine operating point 4: n=3000 r/min, ϕ=1

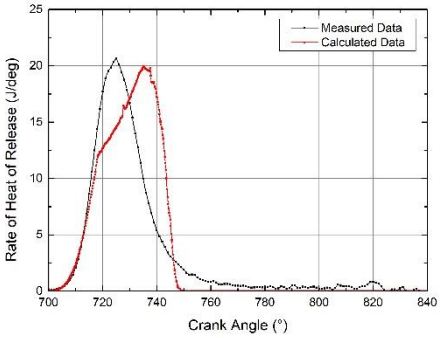

Figure 5-35 Comparison of simulated and measured heat release rate of the engine operating point 4: n=3000 r/min, ϕ=1

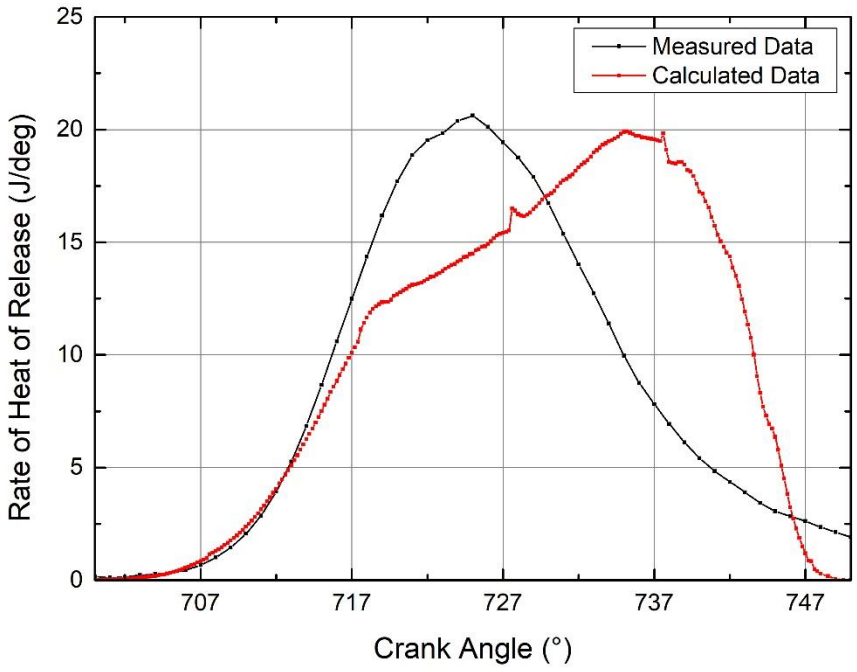

Figure 5-36 Comparison of simulated and measured heat release rate of the engine operating point 4: n=3000 r/min, ϕ=1 (rescaling of x-axis)

5.5 Closing remarks

In this chapter, different cases were calculated to evaluate the EFTM model. Two academic cases were used to validate the implementation of the Eulerian Flame Tracking Model into AVL FIRE™. Then the laminar outwardly spherical propagating flame in a constant-volume cylindrical combustion vessel was simulated to evaluate the prediction ability of the model in the laminar combustion area. After that, one geometry-simple but very typical engine case, i.e. the pancake engine was employed. The simulated in-cylinder pressure histories and the heat release rate were compared with the experimental data. In the last section, simulation results of a single-cylinder DISI engine were presented and analyzed. The main conclusions are summarized in the following:

1) Through the investigation of two academic cases, the successful implementation of the Eulerian Flame Tracking Model was validated. The mean flame front is very smooth, the flame surface keeps as a sphere, and the mean progress variable looks reasonable.
2) Since the reinitialization scheme is performed at the end of every time step in a transient run, errors in the flame front reconstruction accumulate with the increase of the number of calculation steps. This can lead to an unphysical propagation of the flame front and to a wrinkled surface. Therefore, in order to get reasonable results, the CFL number should be kept near to unity. Special focus should be put on a good mesh generation.
3) The model is not sensitive to the mesh topology, when the element volumes of

different topology strategies are similar to each other. This is quite convenient for users, since the generated meshes can differ from one user to another.

4) Compared to the Ewald model, the GFWI model could reproduce the combustion process in the cylinder better by taking the quenching and near-wall turbulence effects into account. The decreasing of the turbulent flame burning velocity when flame front propagates near the wall is physically reasonable.
5) The combination of the heat release analysis and the 1D gas exchange simulation is proved to be a feasible approach to determine the correct boundary conditions for the 3D simulation, which was validated by the very good agreement between the simulated cylinder pressure histories and the experimental data.
6) The EFTM model is able to represent the complex combustion process in a DISI engine for a wide range of operating conditions. The cylinder pressure traces were in good agreement with the experimental data. The mean flame front position at different crank angles were reasonable and reproduced the combustion process in the combustion chamber. However, the simulated heat release rate had an obvious deviation from the measured data. This was caused by the inconsistent flow field characteristics after the rezoning. Therefore, the special care should be put into the numerical techniques to solve this rezone phenomena in the future work.

6 Summary

In the framework of this thesis, the new combustion model, i.e. the Eulerian Flame Tracking Model was implemented to the 3D-CFD tool AVL FIRE™. This is a level-set based flamelet model for the simulation of the turbulent premixed combustion.

At the beginning, the mathematical description of the premixed turbulent combustion was given. The physics of the laminar and turbulent combustion were presented, in order to provide an overview for the following model set-up. Afterwards, the characteristics of combustion phenomena in different regimes were analyzed. By introducing the basic knowledge of the level set method, the G-equation was derived. Two different velocity methods were discussed and compared.

Two numerical cases were investigated to assess the implementation of the model. The numerical error was proved to be sensitive to reinitialization steps. Therefore, in order to increase the accuracy and robustness of the model, the CFL number should be controlled to be near unity. The simulation results of the academic cases showed that the model is able to correctly predict the flame front evaluation. The flame surface can keep as a sphere in a zero-velocity field and the mean reaction progress variable looks reasonable. As long as the volume of the mesh elements is similar, EFT model is not sensitive to the topology strategies.

The next step of the model validation was based on the combustion vessel case. An outwardly spherically propagating laminar flame in a constant-volume cylindrical vessel was widely used for the measurement of the laminar flame burning velocity. Combining with the Schlieren images recorded by the high-speed camera, the flame front at different instants can be obtained, which are ideal for the evaluation of the EFTM. Three cases with different initial pressures, i.e. 0.3 MPa, 0.6 MPa and 1.2 MPa were modeled. The calculated flame front position was in very good agreement with the recorded Schlieren images.

The first turbulent premixed combustion simulation was performed on a geometry-simple SI research engine, pancake engine. The in-cylinder pressure was recorded by a pressure transducer. The moving hexahedron mesh was employed for the numerical setup. The Ewald velocity model and the GFWI velocity model were used to make a cross-comparison. The calculated in-cylinder pressure trace using GFWI model matched the experimental data better. The calculated heat release rate based on the GFWI model validated that the quenching effect should be accounted for in the turbulent combustion modeling again.

Finally, the model was validated by reference to the experimental data for an AVL single-cylinder DISI engine. The gas exchange process was simulated with the combination of results from 1D simulation. The low pressure process was properly predicted in comparison to the measured data. After that, special focus was given to the combustion process. Various engine load points were investigated in order to evaluate the behavior of the model under different engine speeds, equivalence ratios and spark timing variations. In-cylinder pressure histories, the heat release rate and the accumulated heat release achieved an overall agreement to the measured data. It was shown that the EFTM is able to predict the turbulent flame propagation with reasonable accuracy and robustness for a wide range of operating conditions.

However, the deviation of the simulated heat release rate from the measured data was not neglectable. This was caused by the inconsistent flow field characteristics after the rezone procedures. Further improvements of this model should be focused on handling the rezone processes.

The results presented in the framework of this thesis are very encouraging. However, there are still aspects, which have to be addressed and improved in future works. For better prediction, the consistency of the flow field before and after the rezone procedure should be solved. The flame quenching model needs to be further improved and combined with the EFTM. And for further validation purposes, it is necessary to apply this model to other engines with more than one cylinder, where the gas exchange process is much more complicated, and a wide range of operating conditions.

7 References

[1] M. Hirz, “Automotive Engineering for Electrical Engineering and Telematics Fahrzeugtechnik Grundlagen für Elektrotechnik und Telematik,” 2017.

[2] U. S. E. I. Administration, “Annual Energy Outlook 2018 with projections to 2050,” *J. Phys. A Math. Theor.*, vol. 44, no. 8, pp. 1–64, 2018.

[3] C. P, C. P, P. P, A. R, and P. G, “Global carbon atlas,” 2016. [Online]. Available: http://www.globalcarbonatlas.org/en/CO2-emissions.

[4] T. Wei, W. Dong, B. Wu, S. Yang, and Q. Yan, *Influence of recent carbon emissions on the attribution of responsibility for climate change*, vol. 60. 2015.

[5] S. Díaz, J. Miller, P. Mock, R. Minjares, S. Anenberg, and D. Meszler, “Shifting Gears: the Effects of a Future Decline in Diesel Market Share on Tailpipe Co 2 and No X Emissions in Europe,” no. X, 2017.

[6] A. K. Agarwal, A. P. Singh, and R. K. Maurya, “Evolution, challenges and path forward for low temperature combustion engines,” *Prog. Energy Combust. Sci.*, vol. 61, pp. 1–56, 2017.

[7] M. Battistoni, C. N. Grimaldi, V. Cruccolini, G. Discepoli, and M. De Cesare, “Assessment of Port Water Injection Strategies to Control Knock in a GDI Engine through Multi-Cycle CFD Simulations,” SAE Technical Paper, 2017.

[8] S. MARCHESELLI, “CFD in cylinder methodology development for the investigation on correlation between wall wet and soot formation in GDI engine,” 2018.

[9] F. D’Orrico, A. Berton, and M. Sideri, “3D Simulation Methodology for n-Butanol Combustion in an optical accessible research GDI Engine,” *Energy Procedia*, vol. 126, pp. 818–825, 2017.

[10] V. Mittal, D. J. Cook, and H. Pitsch, “An extended multi-regime flamelet model for IC engines,” *Combust. Flame*, vol. 159, no. 8, pp. 2767–2776, 2012.

[11] F. A. Williams, “Progress in knowledge of flamelet structure and extinction,” *Prog. Energy Combust. Sci.*, vol. 26, no. 4, pp. 657–682, 2000.

[12] N. Peters, *Turbulent Combustion*. Cambridge: Cambridge University Press, 2000.

[13] N. Peters, “Laminar flamelet concepts in turbulent combustion,” *Symp. Combust.*, vol. 21, no. 1, pp. 1231–1250, 1988.

[14] M. D. Smoke and V. Giovangigli, “Formulation of the premixed and nonpremixed test problems BT - Reduced Kinetic Mechanisms and Asymptotic Approximations for Methane-Air Flames: A Topical Volume,” M. D. Smooke, Ed. Berlin, Heidelberg: Springer Berlin Heidelberg, 1991, pp. 1–28.

[15] G. E. Andrews and D. Bradley, “Determination of burning velocities: A critical review,” *Combust. Flame*, vol. 18, no. 1, pp. 133–153, 1972.

[16] G. E. Andrews and D. Bradley, “The burning velocity of methane-air mixtures,” *Combust. Flame*, vol. 19, no. 2, pp. 275–288, 1972.

[17] M. Metghalchi and J. C. Keck, “Laminar burning velocity of propane-air mixtures at high temperature and pressure,” *Combust. Flame*, vol. 38, pp. 143–154, 1980.

[18] F. Rahim, M. Elia, M. Ulinski, and M. Metghalchi, “Burning velocity measurements of methane-oxygen-argon mixtures and an application to extend methane-air burning velocity measurements,” *Int. J. Engine Res.*, vol. 3, no. 2, pp. 81–92, Apr. 2002.

[19] A. Moghaddas, C. Bennett, E. Rokni, and H. Metghalchi, “Laminar burning speeds and

flame structures of mixtures of difluoromethane (HFC-32) and 1,1-difluoroethane (HFC-152a) with air at elevated temperatures and pressures," *HVAC&R Res.*, vol. 20, no. 1, pp. 42–50, Jan. 2014.

[20] K. Saeed and C. R. Stone, "Measurements of the laminar burning velocity for mixtures of methanol and air from a constant-volume vessel using a multizone model," *Combust. Flame*, vol. 139, no. 1, pp. 152–166, 2004.

[21] D. Razus, V. Brinzea, M. Mitu, C. Movileanu, and D. Oancea, "Burning Velocity of Propane–Air Mixtures from Pressure–Time Records during Explosions in a Closed Spherical Vessel," *Energy & Fuels*, vol. 26, no. 2, pp. 901–909, Feb. 2012.

[22] M. Mitu, D. Razus, V. Giurcan, and D. Oancea, "Normal burning velocity and propagation speed of ethane–air: Pressure and temperature dependence," *Fuel*, vol. 147, pp. 27–34, 2015.

[23] A. Matsugi, H. Shiina, A. Takahashi, K. Tsuchiya, and A. Miyoshi, "Burning velocities and kinetics of H2/NF3/N2, CH4/NF3/N2, and C3H8/NF3/N2 flames," *Combust. Flame*, vol. 161, no. 6, pp. 1425–1431, 2014.

[24] C. Xiouris, T. Ye, J. Jayachandran, and F. N. Egolfopoulos, "Laminar flame speeds under engine-relevant conditions: Uncertainty quantification and minimization in spherically expanding flame experiments," *Combust. Flame*, vol. 163, pp. 270–283, 2016.

[25] X. J. Gu, M. Z. Haq, M. Lawes, and R. Woolley, "{L}aminar burning velocity and {M}arkstein lengths of methane{/}airmixtures," *Combust. Flame*, vol. 121, no. 1â€“2, pp. 41–58, 2000.

[26] D. Bradley, P. H. Gaskell, and X. J. Gu, "Burning velocities, Markstein lengths, and flame quenching for spherical methane-air flames: A computational study," *Combust. Flame*, 1996.

[27] S. P. Marshall, R. Stone, C. Hegheş, T. J. Davies, and R. F. Cracknell, "High pressure laminar burning velocity measurements and modelling of methane and n-butane," *Combust. Theory Model.*, vol. 14, no. 4, pp. 519–540, Aug. 2010.

[28] K. Saeed and C. R. Stone, "The modelling of premixed laminar combustion in a closed vessel," *Combust. Theory Model.*, vol. 8, no. 4, pp. 721–743, 2004.

[29] F. Mauß and N. Peters, "Reduced kinetic mechanisms for premixed methane-air flames," in *Reduced kinetic mechanisms for applications in combustion systems*, Springer, 1993, pp. 58–75.

[30] N. Peters and B. Rogg, *Reduced kinetic mechanisms for applications in combustion systems*, vol. 15. Springer Science & Business Media, 2008.

[31] P. Clavin and F. A. Williams, "Effects of molecular diffusion and of thermal expansion on the structure and dynamics of premixed flames in turbulent flows of large scale and low intensity," *J. Fluid Mech.*, vol. 116, pp. 251–282, 1982.

[32] D. Linse, *Modeling and Simulation of Knock and Nitric Oxide Emissions in Turbocharged Direct Injection Spark Ignition Engines*. Cuvillier Verlag, 2013.

[33] A. N. Kolmogorov, "A refinement of previous hypotheses concerning the local structure of turbulence in a viscous incompressible fluid at high Reynolds number," *J. Fluid Mech.*, vol. 13, no. 1, pp. 82–85, 1962.

[34] J. D. Buckmaster and G. S. S. Ludford, *Theory of Laminar Flames*. Cambridge: Cambridge University Press, 1982.

[35] N. Chakraborty, "Comparison of displacement speed statistics of turbulent premixed

flames in the regimes representing combustion in corrugated flamelets and thin reaction zones," *Phys. Fluids*, vol. 19, no. 10, p. 105109, Oct. 2007.

[36] V. Sankaran and S. Menon, "Structure of premixed turbulent flames in the thin-reaction-zones regime," *Proc. Combust. Inst.*, vol. 28, no. 1, pp. 203–209, 2000.

[37] H. Pitsch, "A consistent level set formulation for large-eddy simulation of premixed turbulent combustion," *Combust. Flame*, vol. 143, no. 4, pp. 587–598, 2005.

[38] Y. Nada, M. Tanahashi, and T. Miyauchi, "Effect of turbulence characteristics on local flame structure of H 2-air premixed flames," in *TSFP DIGITAL LIBRARY ONLINE*, 2003.

[39] L. P. H. de Goey, T. Plessing, R. T. E. Hermanns, and N. Peters, "Analysis of the flame thickness of turbulent flamelets in the thin reaction zones regime," *Proc. Combust. Inst.*, vol. 30, no. 1, pp. 859–866, 2005.

[40] N. Chakraborty, M. Klein, and R. S. Cant, "Stretch rate effects on displacement speed in turbulent premixed flame kernels in the thin reaction zones regime," *Proc. Combust. Inst.*, vol. 31, no. 1, pp. 1385–1392, 2007.

[41] F. E. Marble, "The Coherent Flame Model of the Turbulent Chemical Reactions," *Acta Astronaut.*, vol. 4, pp. 291–391, 1977.

[42] A. S. Wu and K. N. C. Bray, "A coherent flame model of premixed turbulent combustion in a counterflow geometry," *Combust. Flame*, vol. 109, no. 1–2, pp. 43–64, 1997.

[43] P. Boudier, S. Henriot, T. Poinsot, and T. Baritaud, "A model for turbulent flame ignition and propagation in spark ignition engines," in *Symposium (International) on Combustion*, 1992, vol. 24, no. 1, pp. 503–510.

[44] J. M. Duclos, T. Baritaud, and A. Fusco, "Modeling turbulent combustion and pollutant formation in stratified charge SI engines," *Rev. l'Institut Français du Pétrole*, vol. 52, no. 5, pp. 541–552, 1997.

[45] J. P. Duclos, M. Zolver, and T. Baritaud, "3D modeling of combustion for DI-SI engines," *Oil Gas Sci. Technol.*, vol. 54, no. 2, pp. 259–264, 1999.

[46] S. Bougrine, S. Richard, and D. Veynante, "Modelling and Simulation of the Combustion of Ethanol blended Fuels in a SI Engine using a 0D Coherent Flame Model," SAE Technical Paper, 2009.

[47] K. N. C. Bray and J. B. Moss, "A unified statistical model of the premixed turbulent flame," *Acta Astronaut.*, vol. 4, no. 3–4, pp. 291–319, Mar. 1977.

[48] K. N. C. Bray, P. A. Libby, and J. B. Moss, "Unified modeling approach for premixed turbulent combustion—Part I: General formulation," *Combust. Flame*, vol. 61, no. 1, pp. 87–102, 1985.

[49] K. N. C. Bray, M. Champion, P. A. Libby, and N. Swaminathan, "Finite rate chemistry and presumed PDF models for premixed turbulent combustion," *Combust. Flame*, vol. 146, no. 4, pp. 665–673, 2006.

[50] E. Schneider, A. Maltsev, A. Sadiki, and J. Janicka, "Study on the potential of BML-approach and G-equation concept-based models for predicting swirling partially premixed combustion systems: URANS computations," *Combust. Flame*, vol. 152, no. 4, pp. 548–572, 2008.

[51] S. B. Pope, "Turbulent flows." IOP Publishing, 2001.

[52] J. Janicka, W. Kolbe, and W. Kollmann, "Closure of the transport equation for the probability density funcfion of turbulent scalar fields," *J. Non-Equilibrium Thermodyn.*,

vol. 4, no. 1, pp. 47–66, 1979.

[53] B. Baldwin and T. Barth, “A one-equation turbulence transport model for high Reynolds number wall-bounded flows,” in *29th Aerospace Sciences Meeting*, 1991, p. 610.

[54] S. B. Pope, “PDF methods for turbulent reactive flows,” *Prog. Energy Combust. Sci.*, vol. 11, no. 2, pp. 119–192, 1985.

[55] S. S. Girimaji, “Assumed β-pdf model for turbulent mixing: Validation and extension to multiple scalar mixing,” *Combust. Sci. Technol.*, vol. 78, no. 4–6, pp. 177–196, 1991.

[56] A. R. Kerstein, “A linear-eddy model of turbulent scalar transport and mixing,” *Combust. Sci. Technol.*, vol. 60, no. 4–6, pp. 391–421, 1988.

[57] V. Sankaran, T. G. Drozda, and J. C. Oefelein, “A tabulated closure for turbulent non-premixed combustion based on the linear eddy model,” *Proc. Combust. Inst.*, vol. 32, no. 1, pp. 1571–1578, 2009.

[58] S. Menon and A. R. Kerstein, “The Linear-Eddy Model BT - Turbulent Combustion Modeling: Advances, New Trends and Perspectives,” T. Echekki and E. Mastorakos, Eds. Dordrecht: Springer Netherlands, 2011, pp. 221–247.

[59] S. Menon and W. H. Calhoon Jr, “Subgrid mixing and molecular transport modeling in a reacting shear layer,” in *Symposium (International) on Combustion*, 1996, vol. 26, no. 1, pp. 59–66.

[60] T. Smith and S. Menon, “Model simulations of freely propagating turbulent premixed flames,” in *Symposium (International) on Combustion*, 1996, vol. 26, no. 1, pp. 299–306.

[61] A. W. Cook, J. J. Riley, and G. Kosály, “A laminar flamelet approach to subgrid-scale chemistry in turbulent flows,” *Combust. Flame*, vol. 109, no. 3, pp. 332–341, 1997.

[62] N. Peters and M. Dekena, “Combustion modeling with the G-equation,” *Oil Gas Sci. Technol.*, vol. 54, no. 2, pp. 265–270, 1999.

[63] F. Williams, “3. Turbulent Combustion,” in *The Mathematics of Combustion*, Society for Industrial and Applied Mathematics, 1985, pp. 97–131.

[64] N. Peters, “A spectral closure for premixed turbulent combustion in the flamelet regime,” *J. Fluid Mech.*, vol. 242, pp. 611–629, 1992.

[65] J. . Osher, S.;Sethian, “Fronts Propagating with Curvature Dependent Speed: Algorithms Based on Hamilton-Jacobi Formulations,” *J. Comput. Phys.*, vol. 79, pp. 12–49, 1988.

[66] J. A. Sethian, F. M. Methods, F. M. Methods, and F. M. Methods, “Advancing Interfaces: Level Set and Fast Marching Methods.”

[67] S. Osher and R. Fedkiw, *Level Set Methods and Dynamic Implicit Surfaces*, vol. 153. 2003.

[68] D. Bradley, A. K. C. Lau, M. Lawes, and F. T. Smith, “Flame stretch rate as a determinant of turbulent burning velocity,” *Phil. Trans. R. Soc. Lond. A*, vol. 338, no. 1650, pp. 359–387, 1992.

[69] H. Kobayashi, T. Tamura, K. Maruta, T. Niioka, and F. A. Williams, “Burning velocity of turbulent premixed flames in a high-pressure environment,” in *Symposium (International) on Combustion*, 1996, vol. 26, no. 1, pp. 389–396.

[70] J. Ewald and N. Peters, “A Level Set Based Flamelet Model for the Prediction of Combustion in Spark Ignition Engines Unsteady Premixed Combustion Model,” *Int. Multidimens. Engine Model. User’s Gr. Meet.*, pp. 1–6, 2005.

[71] R. G. Abdel-Gayed and D. Bradley, “A two-eddy theory of premixed turbulent flame propagation,” *Phil. Trans. R. Soc. Lond. A*, vol. 301, no. 1457, pp. 1–25, 1981.

[72] G. Damköhler, “Der einfluss der turbulenz auf die flammengeschwindigkeit in gasgemischen,” *Berichte der Bunsengesellschaft für Phys. Chemie*, vol. 46, no. 11, pp. 601–626, 1940.

[73] J. Ewald and N. Peters, “A level set based flamelet model for the prediction of combustion in spark ignition engines,” in *15th International Multidimensional Engine Modeling User’s Group Meeting, Detroit, MI*, 2005.

[74] J. Ewald, *A level set based flamelet model for the prediction of combustion in homogeneous charge and direct injection spark ignition engines*. Cuvillier, 2006.

[75] D. Suckart and D. Linse, “Modelling turbulent premixed flame–wall interactions including flame quenching and near-wall turbulence based on a level-set flamelet approach,” *Combust. Flame*, vol. 190, pp. 50–64, 2018.

[76] P. Keller-Sornig, *Berechnung der turbulenten Flammenausbreitung bei der ottomotorischen Verbrennung mit einem Flamelet-Modell*. Shaker, 1997.

[77] M. Dekena, *Numerische Simulation der turbulenten Flammenausbreitung in einem direkt einspritzenden Benzinmotor mit einem Flamelet-Modell*. na, 1998.

[78] Z. Tan and R. Reitz, “Development of G-Equation combustion model for direct injection SI engine simulations,” *13th Int. Multidim. Engine Model. User’s Gr. …*, pp. 2–7, 2003.

[79] L. Liang and R. D. Reitz, “Spark ignition engine combustion modeling using a level set method with detailed chemistry,” SAE Technical Paper, 2006.

[80] S. Yang, R. D. Reitz, C. O. Iyer, and J. Yi, “Improvements to combustion models for modeling spark-ignition engines using the G-equation and detailed chemical kinetics,” *SAE Int. J. Fuels Lubr.*, vol. 1, no. 1, pp. 1009–1025, 2009.

[81] D. Linse, C. Hasse, and B. Durst, “An experimental and numerical investigation of turbulent flame propagation and flame structure in a turbo-charged direct injection gasoline engine,” *Combust. Theory Model.*, vol. 13, no. 1, pp. 167–188, Jan. 2009.

[82] H. Lu, “Fundamental Research on Dilution Combustion Characteristics Based on High Energy Ignition,” Tongji University, 2017.

[83] A. C. Alkidas, “Heat Transfer Characteristics of a Spark-Ignition Engine,” *J. Heat Transfer*, vol. 102, no. 2, pp. 189–193, May 1980.

[84] Z. Tan and R. D. Reitz, “Modeling Ignition and Combustion in Spark- Ignition Engines Using a Level Set Method Reprinted From : Modeling of SI Engines,” no. 724, 2003.

[85] Z. Han and R. D. Reitz, “A temperature wall function formulation for variable-density turbulent flows with application to engine convective heat transfer modeling,” *Int. J. Heat Mass Transf.*, vol. 40, no. 3, pp. 613–625, 1997.

[86] T. Kuo and R. Reitz, “Computation of premixed-charge combustion in pancake and pent-roof engines,” 1989.

[87] S. Toninel, H. Forkel, T. Frank, B. Durst, C. Hasse, and D. Linse, “Implementation and Validation of the G-equation Model Coupled with Flamelet Libraries for Simulating Premixed Combustion in I.C. Engines,” *SAE Int. J. Engines*, vol. 2, no. 1, pp. 674–690, 2009.

[88] N. G. Kafoussias and E. W. Williams, “Thermal-diffusion and diffusion-thermo effects on mixed free-forced convective and mass transfer boundary layer flow with temperature dependent viscosity,” *Int. J. Eng. Sci.*, vol. 33, no. 9, pp. 1369–1384, 1995.